A Comparison of Autonomous Navigation Methods for Earth-Moon Halo Orbits

Colin M. O'Leary

Thesis submitted to the Faculty of the
Virginia Polytechnic Institute and State University
in partial fulfillment of the requirements for the degree of

Master of Science
in
Aerospace Engineering

Riley M. Fitzgerald, Chair
Mark L. Psiaki
Shane D. Ross

May 9, 2025
Blacksburg, Virginia

Keywords: Autonomous Navigation, Earth-Moon L1 Halo Orbits, Unscented Kalman Filter

A Comparison of Autonomous Navigation Methods for Earth-Moon Halo Orbits

Colin M. O'Leary

(ABSTRACT)

In this study, we examine three different methods of performing autonomous lunar orbit determination. These methods were the star occultation method, the optical navigation method, and the lunar mirror method. We sought to compare their effectiveness to one another for satellites in northern halo orbits at the L_1 Lagrange point of the Earth-Moon system. six sets of initial conditions were propagated for 30 days using STK. In order to study the fundamental problem of estimation in these orbits, it was assumed that the satellites perfectly maintain their position in the halo orbit (we also did not "bump" them off the orbit with process noise, and instead added random error scaled on our process noise covariance to our estimate). True measurements were also obtained from STK for each measurement model, and then perturbed according to noise models derived from realistic sensor values. Random acceleration perturbations were injected to our dynamics model according to our process noise. All results were obtained via propagation through an augmented unscented Kalman filter (UKF). The optical navigation method outperformed the other methods for each of our test cases, with the occultation, mirror, and optical methods achieving typical steady-state median position accuracies of $8 \times 10^{-2}\,\mathrm{km}$, $1 \times 10^{-1}\,\mathrm{km}$, and $4 \times 10^{-3}\,\mathrm{km}$ respectively. It is also noted that the star occultation method performs well on the test cases with a small perilune distance, as more measurements can be collected. The lunar mirror method also seemed to be particularly sensitive to a high apolune distance, and it is thought that this is due to a high dilution of precision.

A Comparison of Autonomous Navigation Methods for Earth-Moon Halo Orbits

Colin M. O'Leary

(GENERAL AUDIENCE ABSTRACT)

With a renewed interest in lunar travel on the horizon, it is becoming clear that our current methods of satellite tracking for spacecraft around the Moon are unequipped to handle this increase in demand. Therefore, a reliable method of performing autonomous navigation in lunar space is required to facilitate this new interest. Many methods of performing this autonomous navigation have been devised, but little work has been done to compare these methods to one another using standardized, relevant test conditions. In this study, we compared three different methods of performing autonomous navigation in six different test cases. The methods being tested were the star occultation method, the optical navigation method, and the lunar mirror method. These six test cases were a selection of halo orbits in the Earth-Moon system (a set of sensitive orbits dependent on Earth-Moon dynamics). We simulated the true state information for each of these test cases for a period of 30 days. We also simulated the true values of the measurements that would have been obtained by each of our three methods using this same software. Then to test the methods, we propagated the initial state of each test case using an estimator equipped with one of our measurement methods under test. This was repeated for each method, for a total of 18 test results. It was found that the optical navigation method was the best performing for all six of our test cases.

Dedication

Dedicated to all those who believed in me, even when I didn't.

Acknowledgments

I would like to thank my car. It has been my faithful steed for nearly a decade, and without it I literally could not have gotten here today. Here's to another 105 000 miles buddy!

I would like to thank my Brazilian jiu-jitsu gym, Team Mannon BJJ. It has been an amazing "third place" for me to make new friends, and to get in shape. This place helped me pull out of a dark time of my life.

I would like to thank Mill Mountain Coffee and Tea. This place has been a comfortable haven for me to rest, recover, and meditate when the stress of life becomes too much to bear.

I would like to thank my loyal friends, for sticking by my side through the thickest of life's troubles. If not for them, I may not have remembered who I truly am.

I owe a big thank you to my advisor, Dr. Fitzgerald. His patience and understanding when life circumstances impacted my ability to work was nothing less than saintly. He is an amazing teacher, mentor, and friend. I truly could not have asked for a better advisor.

Finally, I want to thank my family. They have always been there to listen, push me along, and help me find my way in even the bleakest of times. I would not be where I am today without their unwavering support.

Contents

List of Figures

List of Tables

List of Abbreviations

CR3BP Circular Restricted Three-Body Problem

DSN Deep Space Network

ESA European Space Agency

GDOP Geometric Dilution of Precision

GNSS Global Navigation Satellite System

HAST High Accuracy Star Tracker

ICRF International Celestial Reference Frame

IMU Inertial Measurement Unit

JPL Jet Propulsion Laboratory

LEO Low Earth Orbit

LIAISON Linked, Autonomous, Satellite Orbit Navigation

LRRR Lunar Ranging Retroreflector

LRS Laser Ranging System

NASA National Aeronautics and Space Administration

RMS Root Mean Square

STK Systems Tool Kit

UKF Unscented Kalman Filter

Chapter 1

Introduction

Humanity's interest in the Moon has been renewed in a manner not seen since the Space Race. NASA and ESA have plans to have people land on the Moon by 2025, with plans to set up an orbiting lunar base soon afterward [19][4]. However, sustained operations in cislunar space will not be possible without a reliable lunar autonomous navigation system. Currently, we can perform station-keeping on objects in cislunar space using the Deep Space Network (DSN), but this system will become overwhelmed as the volume of missions to the Moon increases.

This begs the question, how should one perform autonomous navigation for orbits in cislunar space? Answering this question is key to reducing our reliance on the DSN, and opens the doorway to establishing a GNSS-like (Global Navigation Satellite System) constellation on the Moon. GNSS constellations on Earth trivialize performing accurate positioning estimation, and replicating such a system on the Moon would be a scalable, long-term solution for navigation in lunar space. However, a GNSS-like constellation cannot exist on the Moon without a reliable way to perform autonomous lunar orbit determination; our GNSS systems on Earth rely on ground-based stations to station-keep the satellites in the constellations, which is not currently feasible on the Moon.

Finding a way to perform autonomous lunar orbit determination is a problem that has been worked on for over 40 years, and many methods have been devised for doing so. Some examples include Born's LIAISON navigation method [20], Psiaki's star occultation method

[30], and the optical navigation method used for interplanetary navigation during Orion's missions to the Moon [17]. However, little work has been done to compare these methods to one another in a standardized environment, and some have never been tested in halo orbits.

1.1 Lunar Space and Halo Orbits

A halo orbit is a periodic, non-planar orbit associated with a Lagrange point between two celestial bodies. Crucially, they are orbits that cannot be described with two-body problem dynamics, which means that many proven methods for performing orbit determination cannot be relied upon. An artistic rendering of multiple families of halo orbits can be seen in Fig. 1.1. Halo orbits are highly useful for scientific exploration despite their added complexities when compared to standard orbits, and NASA even has plans for the near future to construct a lunar base (called Gateway) in a halo orbit [4].

Halo orbits are attractive orbits for satellites that we launch for scientific exploration because they do not revolve around a central body. By not revolving around a central body, the satellite in the halo orbit is always visible from Earth in most cases, and has constant viewing/communication geometry with the Moon's surface. Some examples of research satellites that are already in halo orbits are Queqiao (a Chinese communications relay satellite that is in a halo orbit around the L_2 Lagrange point of the Earth-Moon system such that it can always see the dark side of the Moon as well as Earth) and the James Webb Space Telescope (in a halo orbit around the L_2 Lagrange point of the Sun-Earth system) [37][5]. For how important halo orbits are becoming to scientific discovery, it is more important than ever to investigate how the autonomous navigation methods we rely on function in these environments. Moreover, they will serve as a challenging but relevant unified test case for the considered navigation methods.

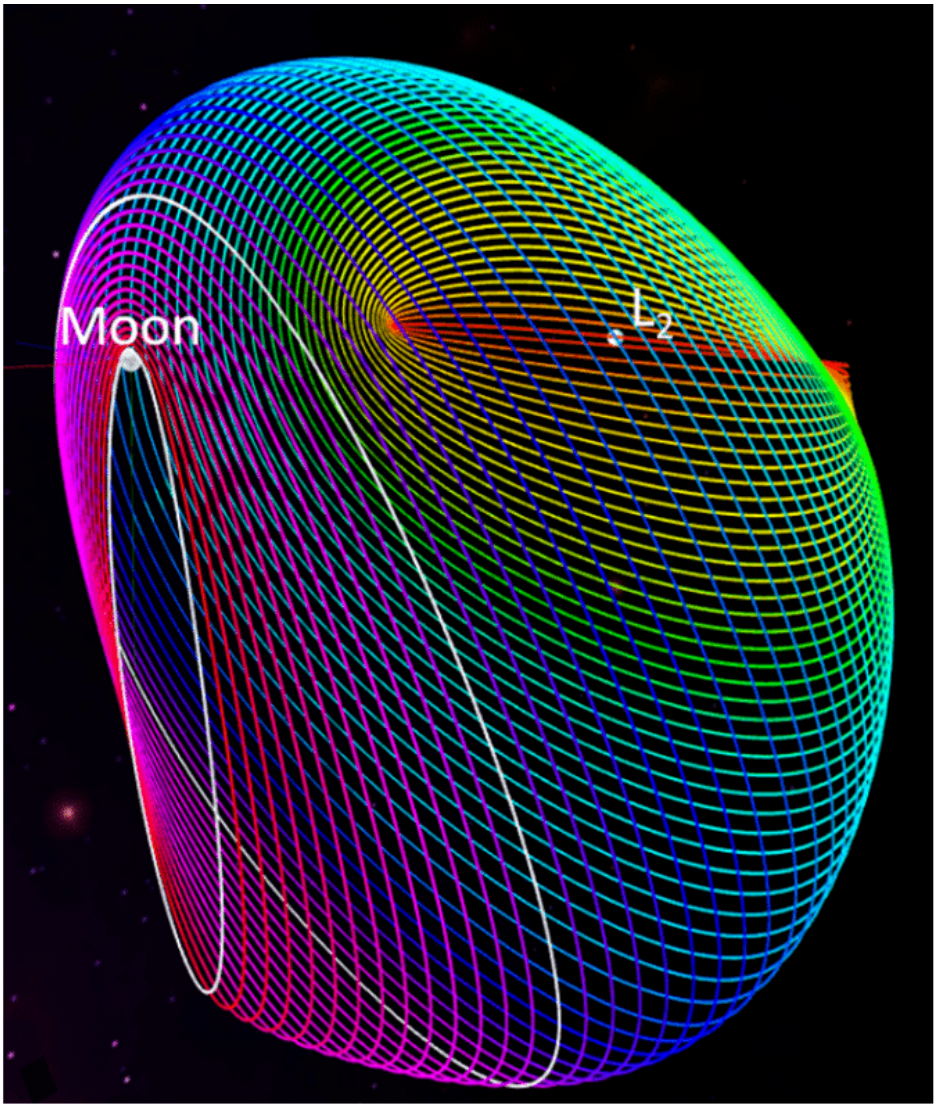

Figure 1.1: The L_1 and L_2 Halo Orbit Families, as well as the Near-Rectilinear Halo Orbits (caption and photo reproduced from [34])

1.2 Outline

Chapter 1: In the introduction, we looked at the context that surrounds this problem. We discussed how there has been a revitalization in the interest of travel to the Moon, and briefly discussed how this revitalization has caused strain on the existing systems we use for tracking spacecraft. This strain necessitates the discovery and perfection of a more reliable long-term solution. Finally, we discussed the relevance of halo orbits as a unifying test case.

Chapter 2: In the literature review section, we will summarize what work has been done on finding autonomous navigation methods for spacecraft in cislunar space. The methods that will be used in this study will be introduced, and a comparison study involving one of the methods we used that has already been done will be examined. We also will discuss in greater depth how navigation in this region of space has been done in the past, and why they may not be reliable going forward.

Chapter 3: In the methodology section, we will walk through how our chosen methods function from a theoretical perspective. We will also discuss how each of these methods had their true measurement values simulated for each of our test cases, and how realistic models for the uncertainty of these measurements were derived as well as applied. We also will discuss in detail the dynamics model we used, how we performed our coordinate transformations, and how our true state information for each of our test cases was propagated. A walkthrough of the augmented unscented Kalman filter (UKF) that was used to gather all of our results will be provided here.

Chapter 4: In the results and discussion section, we will cover our test conditions used to gather our results in great detail. This will include covering the initial conditions of our halo orbits, the specifications of hardware we used to simulate the performance of real sensor systems, and the precise values of constants we had to use to collect our data. After this, we

will present the results of how each method performed in our test cases, and compare their performances to one another. We will examine graphs of interesting cases, and a data table that summarizes the method's performance in all cases will be provided for each method. Graphs that depict the results of every method for every test case can be found in Appendix A.

Chapter 5: Finally, we will cover what we have learned in the conclusions section. We will discuss our main takeaways from this study, its limitations, and ideas for how work in this field could be continued in the future. We also will make specific recommendations about which methods to use in a given orbit based on our data.

Chapter 2

Literature Review

Autonomous lunar orbit determination is a concept that has been around for decades, but has only recently become a practical consideration in light of the increased interest in sustained lunar exploration. Thus, many methods have been proposed for achieving this.

First we will outline the current methods used for navigation in lunar space, as well as proposed future large-scale methods. Finally, we will explore some proposed autonomous methods and what work has already been done to compare them to one another.

2.1 Using GNSS in Lunar Space

Using GNSS signals from satellites on the opposite side of the Earth to perform navigation in high-altitude orbits is an idea explored in this paper [36]. In Fig. 2.1, we can see the different regions of GNSS satellite coverage and how they extend past the Earth.

In Winternitz' paper, the usage of GNSS navigation in orbits with apogee distances of 12 and 25 Earth radii is discussed (referred to as "Orbit A" and "Orbit B" respectively for the remainder of this section) in relation to the four satellites from the Magnetospheric Multiscale (MMS) mission. At the time of publication, data was available on the navigation system's performance for all four satellites in Orbit A, but not in Orbit B. Because of this, the data from Orbit A was extrapolated to estimate the navigation system's performance on Orbit B.

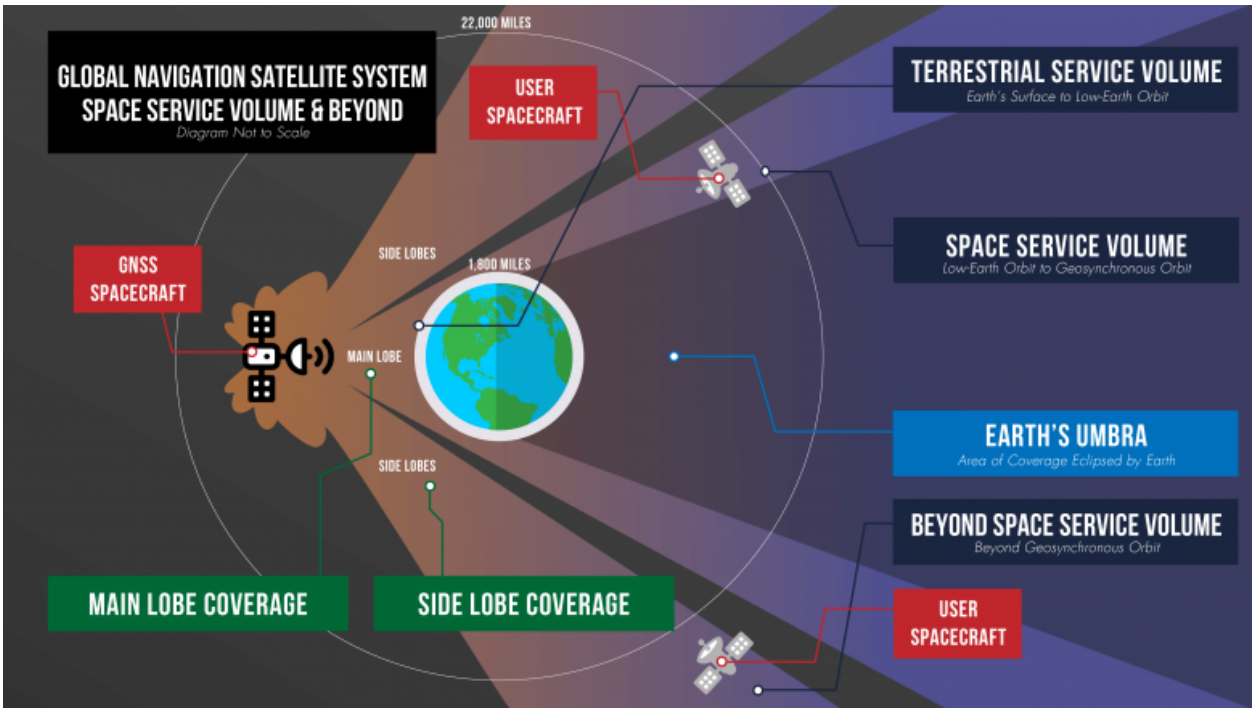

Figure 2.1: A graphic detailing different areas of GNSS coverage (graphic and caption from [11])

For Orbit A, the navigation system for one of the satellites (MMS1) had a moving average of 4 m (99% confidence interval) when above 3 Earth radii in altitude, and a residual sum of squares (RSS) of 65 m; the rest of the satellites performed similarly. The extrapolation of these results for Orbit B estimate that a moving average of 20 m (99% confidence interval) when above 3 Earth radii, and a RSS of 150 m can be expected.

The accuracy values for the MMS navigation system show that using GNSS for navigation is a valid solution for even the most highly elliptical of Earth-focused orbits, though this will be an insufficient method for our halo orbits. The distance between the Earth and the Moon is approximately 60 Earth radii on average, and the shadow casted by Earth's umbra (see Fig. 2.1) will mean that our satellites in halo orbits will receive little to no GNSS measurements because of their immense distance from the Earth. This immense distance also means that the geometric dilution of precision (GDOP) would be high enough that

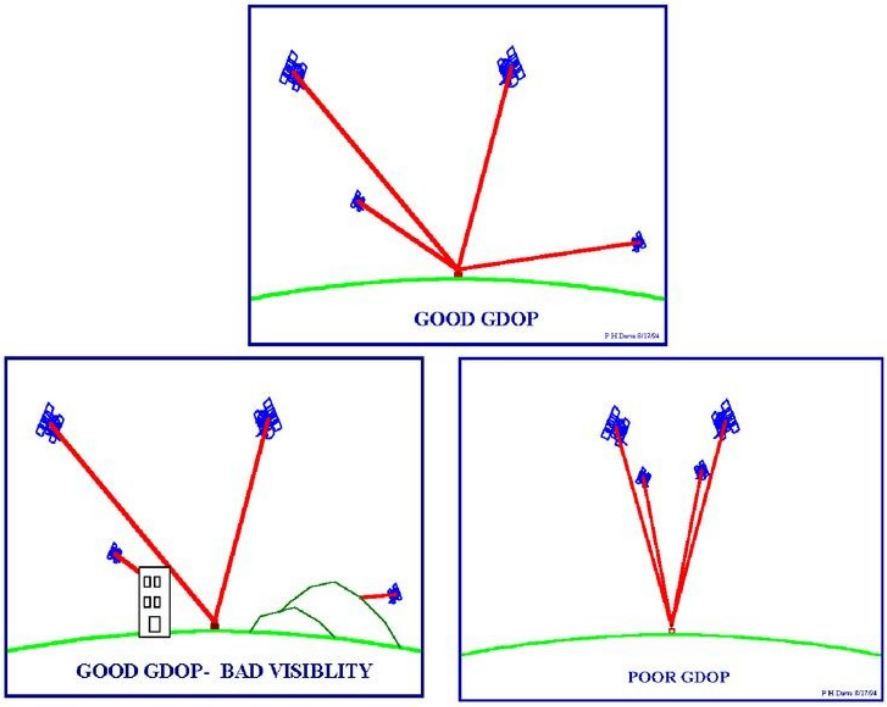

Figure 2.2: A graphic depicting what the difference is between good GDOP and bad GDOP (graphic from [27])

sufficiently accurate navigation would likely be unachievable even if GNSS measurements could be received (i.e., the GNSS satellites would be so far away that measurements from them would not be distinct enough from one another to observe the satellite's entire state). In Fig. 2.2, the difference between good GDOP and bad GDOP is explained. The top graphic represents an ideal case for GNSS navigation, the bottom-left graphic describes how bad visibility of the satellites can lead to large navigation errors (as would be the case if our satellites in halo orbits spent most or all of their time in Earth's umbra), and the bottom-right graphic shows how bad GDOP can also lead to large navigation errors even with perfect visibility (as would be the case for our satellites in halo orbits even if the Earth somehow did not obstruct our view of the GNSS satellites). This means it is clear that simply using GNSS will not be feasible for orbits in this region.

Figure 2.3: Deep Space Network, Deep Space Station 35 (DSS-35) at the Canberra Deep Space Communications Complex near Canberra, Australia (picture and caption from [26])

2.2 Deep Space Network

The Deep Space Network (DSN) is a network of ground-based facilities that are used for tracking and communicating with spacecraft, as well as for gathering scientific observations. In service since 1958, the DSN was originally established to receive telemetry and plot the orbit of the Explorer 1 (the first successful US satellite). Later that year, the Jet Propulsion Laboratory (JPL) was transferred to the control of the newly-created NASA, and management of the DSN was transferred alongside it. Shortly after this transfer, NASA formally established the DSN as its own program that was aimed at accommodating all deep space missions. Since then, it has become a vital part of countless space missions, including both deep space missions and select Earth-orbiting missions. It even aided in communication and tracking of Apollo spacecraft. DSN currently consists of three facilities located in California, Spain, and southeast Australia [3]. A picture from the DSN facility in Australia can be seen in Fig. 2.3. These locations were strategically chosen such that one

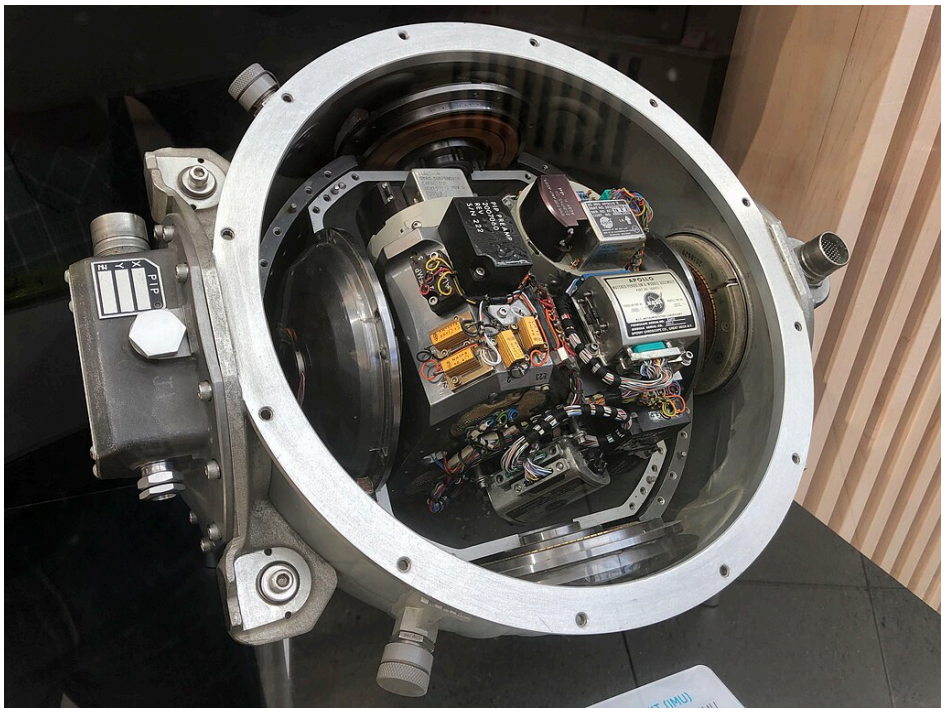

Figure 2.4: Apollo's IMU [32]

facility is always able to view a spacecraft, allowing for seamless tracking and communication. However, due to the recent increase in lunar missions and decreased budgets for the DSN's operation, it is having a hard time keeping up with demand [18]. This problem is compounded by DSN's aging infrastructure. During the Artemis I mission, a particularly intensive one for the DSN, science missions lost 1585 hours of DSN time (this includes the James Webb telescope, which lost 185 hours alone) [18]. Such a loss could be disastrous with a crewed mission, and with the number of lunar missions only expected to increase in both number and complexity, it is clear that future lunar missions should not rely on the DSN.

2.3 Inertial Measurement Navigation

It could be asked why we need to invest in autonomous navigation when one could simply use an inertial measurement unit (IMU) to maintain your state after being given an initial position and velocity. A star camera could also be used in conjunction with an IMU to provide reliable and accurate data for orientation. Dating back to the Apollo missions (Apollo's guidance system can be seen in Fig. 2.4), IMUs have been used on space missions. Modern IMUs that are used on Mars rovers (including the Perseverance from 2020) are solid state, meaning they can be relied upon for upwards of 20 years [23]. The drawback of IMUs is that they accrue error over time due to their navigation being based on dead reckoning. This means that even the best of IMUs will eventually become unreliable after enough time has passed. This may not be a problem with missions that aim to land on the Moon, but will certainly be a problem for missions that aim to orbit the Moon. Another major drawback is that IMUs cannot detect gravitational acceleration when the spacecraft is in-flight, so they must be supported by highly accurate gravity models and external tracking from something akin to the DSN. This means that using an IMU exclusively for navigation is only a possibility for landing missions and when navigating on the surface of a celestial body (like the rovers on Mars).

2.4 GNSS-like Constellation for the Moon

While using Earth-based GNSS constellations for travel to the Moon is out of the question, as the satellites in these constellations orbit the Earth and orient their signals downward to below the constellation's altitude, constructing a GNSS-like constellation around the Moon is an attractive idea. This idea is one that is attractive to the ESA and NASA, as they

plan to construct a navigation constellation around the Moon [19]. Though, this does not eliminate the need for a method of performing autonomous lunar orbit determination, as the satellites in the navigation constellation cannot be corrected via ground-based stations like they can on Earth [19].

2.5 Autonomous Lunar Orbit Determination Methods

Having identified the need for an autonomous lunar orbit determination method, we will now outline a few proposed methods.

2.5.1 LIAISON Navigation

This paper [20] introduced an autonomous interplanetary orbit determination method that utilizes satellite-to-satellite tracking, and is based on a 1984 paper by Markley [22]. This method, called LIAISON navigation, uses only scalar satellite-to-satellite observations (such as crosslink range) to estimate the orbits of all participating spacecraft. Importantly, this method does not work in near-body orbits that would be dominated by two-body dynamics because asymmetry in the acceleration field is essential for this method to function. This method also does not function well when satellites do not have large separations between one another, when the satellites are in coplanar orbits, or when satellites are separated purely in the z-direction. Performance with this method is optimized with as many satellites in the network as possible, and on orbits with shorter periods. This method's efficacy was analyzed on spacecraft in halo orbits near the L_1 Lagrange point of the Earth-Moon system utilizing the circular restricted three-body problem. Navigation accuracy varied between 5 m and 40 m depending on the angle of separation between the spacecraft, but were typically

between 5 m and 10 m.

2.5.2 Relative Positioning Method

This paper [31] introduced the relative positioning method for autonomous orbit determination where reliance on GNSS signals was impossible. By using the relative position vector from one spacecraft to another, the 6-element state vector (along with the drag parameter) of both spacecraft can be determined. Importantly, this differs from the LIAISON method because the relative positioning method uses relative position vectors as opposed to using scalar measurements. This method was tested on satellites in LEO, and was found to be more accurate when the spacecraft are further away from each other. Position accuracies on the order of 1 m RMS are obtainable under ideal circumstances.

2.5.3 Star Occultation Method

This paper [30] introduced the star occultation method for use in performing autonomous lunar orbit determination. This method works by using a star camera to measure the time that stars with a known direction set behind or rise above the lunar limb, then feeding these measurements into a Kalman filter. In the near-lunar orbit tested in this paper, the system was highly observable, and demonstrated an absolute position accuracy of 70 m per axis for a near-lunar orbit with a perilune altitude of 314.4 km and an apolune altitude of 315.6 km. In this paper, occultations that occurred on the sunlit side of the Moon were excluded. Because this is one of the measurement methods used in this comparison study, more information on how this measurement method works is discussed in section 3.1.1.

2.5.4 Optical Navigation Method

The optical navigation method is a common method for performing autonomous navigation in beyond-near-body scenarios [17] [15]. This method involves pointing a camera at a known body (such as Earth or the moon) and counting how many pixels it occupies within the camera's field of view. From the amount of pixels occupied by the known body, the distance to that body can be measured and the spacecraft's state estimated. This method was analyzed for use in a lunar transfer trajectory, and it was found that the entry flight path angle could be maintained with an error of 0.27° [17]. This paper [15] further investigates different ellipse-fitting algorithms to see which performs best for this measurement method.

2.5.5 Lunar Mirror Method

This paper [38] proposes a new method of performing autonomous lunar orbit determination. This method relies on on-board laser ranging measurements to lunar ranging retroreflectors (LRRR) estimate the position and velocity of the spacecraft. The LRRRs used in this study were installed on the lunar surface in the 1960s and 1970s during the United States' Apollo missions and the Soviet Union's Luna missions [35], but new LRRRs were installed on the Moon in 2023 (Chandrayaan-3 [24]) and 2025 (Blue Ghost Mission 1 [1]). Each LRRR is designed to reflect light back to its source, and a diagram showing an LRRR is shown in Fig. 2.5. Simulation with a subset of Lyapunov and halo orbits showed that sub-kilometer position estimation is achievable by measuring range to only one mirror at a time. In this study, we will use the same mirrors as Zaffram used in his study, but we will always perform ranging to every mirror within view from our satellite. This means that our study will present a "best case scenario" for our conditions, but ranging to only a single mirror (as done by Zaffram) is a more logistically feasible implementation of this method.

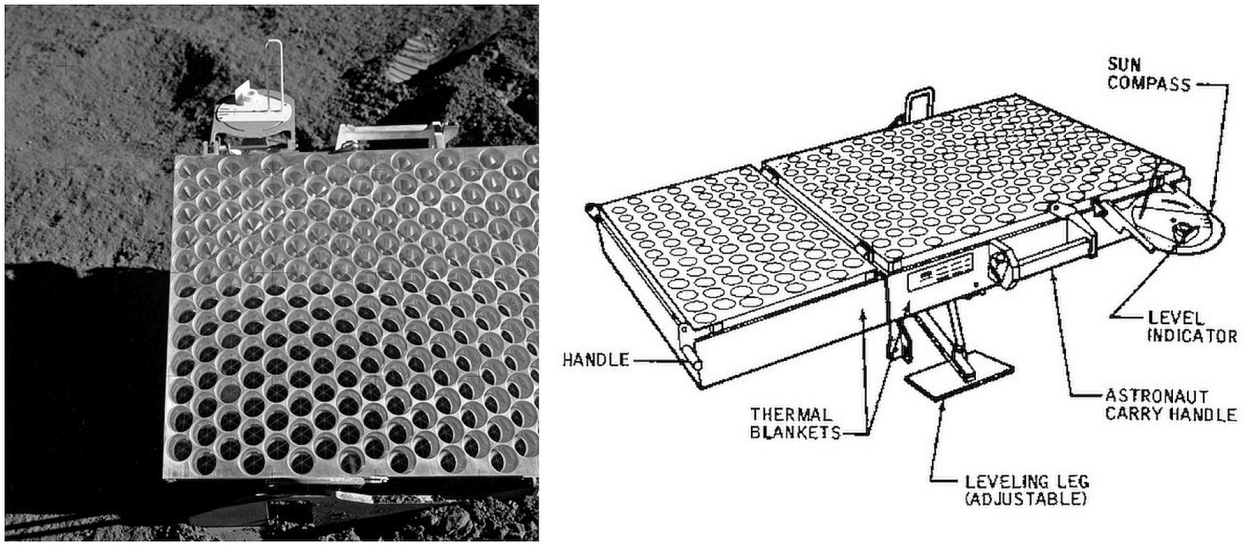

Figure 2.5: The LRRR left on the lunar surface by the Apollo 15 astronauts and a diagram showing its components. The corner cube mirrors that reflect laser light back to its source are clearly seen in the photograph (image and caption from [6]).

2.6 Comparing Different Autonomous Lunar Orbit Determination Methods

This paper [13] directly compares three different methods of performing autonomous lunar orbit determination. The three methods are the aforementioned LIAISON method, star occultation method, and the relative positioning method. To perform this comparison, a high-fidelity truth-model simulation was compared to Kalman filter results produced with each of the three methods. The primary spacecraft's trajectory in this study was in a near-lunar polar orbit with an apolune altitude of 375 km, and a perilune altitude of 300 km. The LIAISON method, star occultation method, and relative positioning method had a steady-state RMS position error magnitude of approximately 2.1 m, 4.6 m, and 4.5 m respectively.

Like this study, this paper [13] also compares three different methods of performing autonomous

lunar orbit determination. Though, Bowman compares the relative positioning method, LIAISON method, and star occultation method, whereas this study will compare the lunar mirror method, optical navigation method, and star occultation method. Bowman's study also directly compared these methods' performance to each other for a satellite in a near-lunar polar orbit. Importantly, while two other satellite trajectories were simulated, including one in a halo orbit, only the aforementioned satellite in a near-lunar polar orbit had all three methods evaluated on it. In this study, the performance of all three methods under test will be examined for six halo orbit trajectories. Bowman's orbital dynamics propagator incorporated a spherical harmonics gravity model, along with solar radiation pressure and lunar surface albedo radiation pressure. In this study, we will use a simpler gravity model afforded to us by the circular restricted three-body problem (though, using a spherical harmonic gravity model is less important for our study due to halo orbits being high-altitude by nature), and we will neglect the effects of solar radiation pressure and lunar surface albedo radiation pressure (though we will not neglect uncertainties caused by these effects). For Bowman's study, a star catalog with 170 total stars was used, whereas our star catalog contains over 9000 stars. It should be noted that our larger star catalog will be necessary since our halo orbits are much further from the Moon, and a star catalog this large would be excessive for orbits that are near-lunar. We also will examine the steady-state 10th, 50th, and 90th percentile errors for both position and velocity, in contrast to steady-state RMS position errors (as used in Bowman's study). This choice was made because our errors have a lot more variation than Bowman's do, and we wanted to capture these regions of higher error while not obscuring the regions of optimal performance of each method. This difference between Bowman's errors and ours is partly due to the variation in the dynamics of the halo orbits over the course of an orbital period as well as using a 30-day testing period as opposed to a 10-day testing period.

Chapter 3

Methodology

In this chapter, we will cover the mathematical processes used in this study. We will start by introducing each method, how we simulated true measurements for that method, then cover how we derived our uncertainty models for that method. Afterwards, we will cover how we used STK to generate truth data for each of our test orbits, our dynamics model, and how we generated quaternions for each test orbit to convert between our needed coordinate frames. Finally, we will provide an in-depth walkthrough of the augmented unscented Kalman filter that served as our estimator for this study.

3.1 Measurement Methods

In this section, we will introduce a measurement method, then cover how the true values for its measurements were simulated, and finally cover how its uncertainty model was derived. This process will be repeated for each of our three measurement methods.

3.1.1 Star Occultation Method

Here, we will introduce the star occultation method, then cover how we simulated our true measurements for this method, then show how we derived this method's uncertainty model.

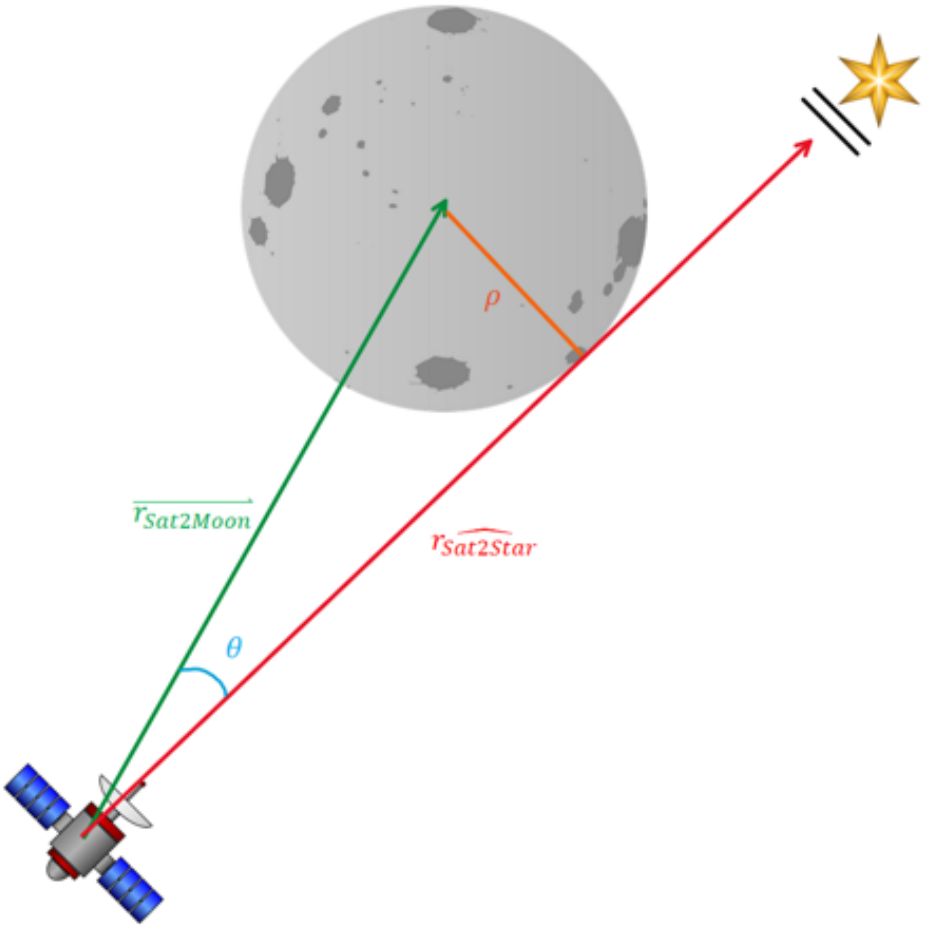

Figure 3.1: Diagram of a star occultation

Method Introduction

Suppose we have a repository of stars that we have astrometric data for. At the moment one of these "known" stars occults, Fig. 3.1 captures the geometry of the situation. For an ideal occultation (which means one without any error in $\vec{r}_{\text{sat2moon}}$, $\hat{r}_{\text{sat2star}}$, or time of occultation) behind a perfectly spherical Moon, ρ should always be equal to the radius of the Moon.

From Fig. 3.1, we can derive Eqns. 3.1–3.4.

$$r_{\text{sat2moon}} = ||\vec{r}_{\text{sat2moon}}||_2 \tag{3.1}$$

$$\hat{r}_{\text{sat2moon}} = \frac{\vec{r}_{\text{sat2moon}}}{r_{\text{sat2moon}}} \tag{3.2}$$

$$\cos\theta = \hat{r}_{\text{sat2moon}} \cdot \hat{r}_{\text{sat2star}} \tag{3.3}$$

$$\rho = r_{\text{sat2moon}} \sin\theta \tag{3.4}$$

Where $\vec{r}_{\text{sat2moon}}$ and $\hat{r}_{\text{sat2star}}$ are given. If our estimate of $\vec{r}_{\text{sat2moon}}$ is perfect at the moment of occultation, then ρ should be equivalent to the radius of the Moon. Therefore, by measuring the time that a known star occults and calculating ρ for this moment in time, we can compare it to the Moon's known radius and improve our estimate of our spacecraft's state. We treat ρ at the time all occultations occur as our measurement vector ($\vec{z}$) for this method. Note that θ is the angle between $\vec{r}_{\text{sat2moon}}$ and $\hat{r}_{\text{sat2star}}$, which can be seen in Fig. 3.1.

For more information on this method or its derivation, please refer to [30].

Truth Measurement Simulation

STK's "bright star catalog" has over 9000 stars [9]. These stars range in visual magnitude from as bright as -1.46, and as dim as 7.96 [9]. This catalog has complete astrometric data for all of these stars and uses the Harvard Revised ID number to differentiate between them [9]. Every single star in this catalog was added to our scenario to be checked for occultations with the Moon.

STK's "access" tool is versatile and can be used for computing many different values in relation to two different STK objects [10]. For our purposes, we applied a "line of sight" (LOS) constraint between our satellite and all of the stars in our scenario. With this, we

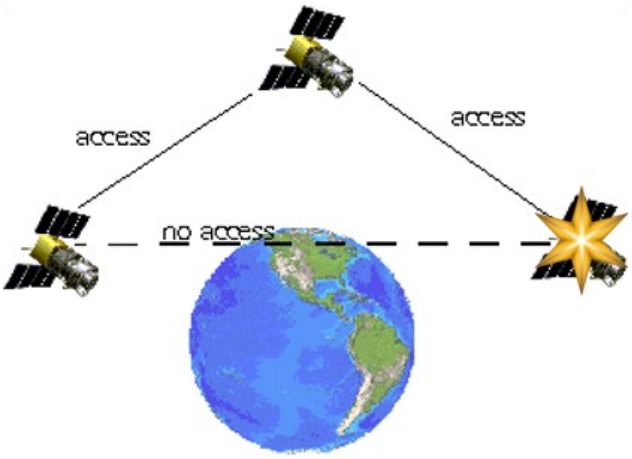

Figure 3.2: STK Access Visualization (Figure from [10])

were able to see when one of these stars had its LOS vector broken, or gained a LOS vector when it previously did not have one. A visual description of this can be seen in Fig. 3.2. This allowed us to see which stars occulted over our data interval, and get accurate information at this time of occultation.

To obtain the true measurements for the star occultation method, we first computed access for all of the stars in STK's bright star catalog. For more information on STK's access tool, please refer to Fig. 3.2.

The time that gaps in visual access from the satellite to a particular star started or stopped were recorded as the times of occultation. The direction vector to each star was also sampled once per day over the testing period, then interpolated to the time of occultation. Star luminosity was also recorded, and occultations that occurred with stars that were too dim for HAST's default settings were excluded. (This value is recorded in Table 4.1 as $L_{\min}$.) For more information on HAST (the star camera specifications used in this study), please refer to section 4.1.2. Occultations were also excluded if more than one occultation occurred in a single time step, or if the direction vector from the satellite to the star ($\hat{r}_{\text{sat2star}}$) and the direction vector from the satellite to the Moon ($\hat{r}_{\text{sat2moon}}$) were not co-directional, which

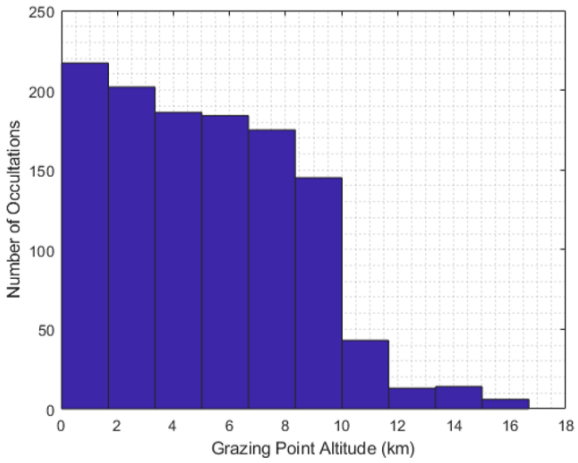

Figure 3.3: A plot showing how many of the occultations reported by STK had grazing point altitudes that were different from zero for Case 4

could occur if visual access was obstructed by a body other than the Moon.

One practical note of caution: It was found that STK had slight inconsistencies when computing occultation times for star objects due to a small issue with the way it computes light travel time from satellites to star objects[1]. This caused the calculated grazing point altitude at the reported time of occultation to be several kilometers off in some cases (see Fig. 3.3 to see the effect of this for Case 4). To find the correct time of occultation, we first defined grazing point altitude as a function of time, seen in Eqn. 3.5 where R_{moon} is the radius of the Moon (recorded in Table 4.1) and ρ is calculated according to Eqn. 3.4.

$$h(t) = \rho(t) - R_{\text{moon}} \tag{3.5}$$

At the precise time of occultation, t_{occult}, it should be true that $h(t_{\text{occult}}) = 0$. This root-finding condition means that finding the precise time of occultation can be treated as a classic root-finding problem. MATLAB's `fzero.m` (which uses a combination of bisection,

[1]As of the time of writing, the small issues found within STK are being addressed under bug IDs ANLY-873, ANLY-874, and ANLY-880.

secant, and inverse quadratic interpolation methods [8]) was then used with STK's reported occultation time as an initial guess to find t_{occult} for each occultation to machine precision.

Uncertainty Model

Once a corrected occultation time was achieved (as discussed in section 3.1.1), central differencing was performed on this same function to determine the change in grazing point altitude with respect to time at the moment of occultation ($\frac{dh}{dt}$). This is illustrated in Eqn. 3.6 where $h(t)$ is grazing point altitude as a function of time (derived in Eqn. 3.5), t_{occult} is the corrected occult time, and Δt is the central differencing parameter (shown in Table 4.1).

$$\frac{dh}{dt} = \frac{h(t_{\text{occult}} + \Delta t) - h(t_{\text{occult}} - \Delta t)}{2\Delta t} \tag{3.6}$$

To relate this sensitivity to the possible error in true radius ρ at time t_{occult}, this was multiplied by the inverse of our star camera's frame rate (i.e., the time between each captured image, t_{frame}, which is shown in Table 4.1) to achieve the uncertainty in our calculated radius. This is shown in Eqn. 3.7.

$$\sigma_R = \frac{dh}{dt} t_{Frame} \tag{3.7}$$

This was squared, and then added to our terrain radius variance ($\sigma^2_{\text{terrain}}$) to generate an R value for each occultation, shown in Eqn. 3.8. This terrain radius variance represents the discrepancy between the most accurate models of the Moon's terrain, and its actual terrain. The value used in this study is documented in Table 4.1.

$$R = \sigma_R^2 + \sigma^2_{\text{terrain}} \tag{3.8}$$

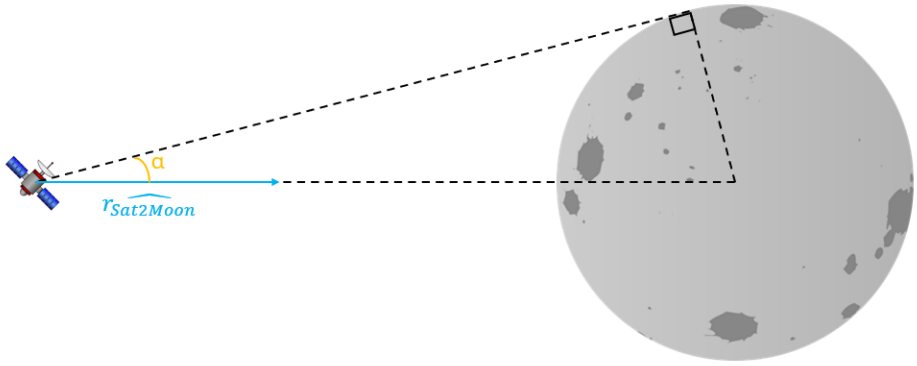

Figure 3.4: Diagram of measurements for use in optical navigation method

3.1.2 Optical Navigation Method

Here, we will introduce the optical navigation method, then cover how we simulated our true measurements for this method, then show how we derived this method's uncertainty model.

Method Introduction

Suppose that we can find α and $\hat{r}_{\text{sat2moon}}$ as seen in Fig. 3.4 using a satellite-mounted star camera. Note that while α is similar to θ as defined in section 3.1.1, its been relabeled here due to its importance in this method.

Finding these values using images from a star camera is covered extensively in [15], but these derivations are outside the scope of this paper. Note that the Moon's center relative to the background stars defines $\hat{r}_{\text{sat2moon}}$, and the apparent size of the Moon in the image defines α. Once these values are obtained, we can find $\vec{r}_{\text{sat2moon}}$ using Eqn. 3.9.

$$\vec{r}_{\text{sat2moon}} = \left(\frac{R_{\text{moon}}}{\sin \alpha} \right) \hat{r}_{\text{sat2moon}} \tag{3.9}$$

In this study, it is assumed that the Moon is a perfect sphere, therefore R_{moon} is a constant

value (R_{moon} is shown in Table 4.1). [15] provides additional information on how to perform these calculations for a non-spherical Moon, and we account for non-spherical effects when calculating our measurement uncertainties for this method (see section 3.1.2).

True Measurement Simulation

Obtaining the true measurements for the optical navigation method was pretty straightforward. The Moon's position was sampled at every second, then the Moon's position was subtracted from the satellite's position to simulate the measurements from the star camera for this method. If the Moon was too close, then the entire Moon would not fit within the frame of the star camera and no measurements would be obtainable. This was accounted for in our simulated measurements.

Uncertainty Model

As the only measurement method tested that had non-scalar measurements, the uncertainty model for the optical navigation method is the most complicated. Our process for deriving this uncertainty model is heavily based on Christian's paper [15]. The measurement noise is assumed to be zero-mean Gaussian with the following covariance:

$$R = \sigma_\rho^2[\hat{r}\hat{r}^T] + \sigma_u^2[I_{3x3} - \hat{r}\hat{r}^T] \tag{3.10}$$

To start, we want to satisfy Eqn. 3.10 in order to calculate our measurement uncertainty matrix for each sample time. The first term in Eqn. 3.10 is the uncertainty in the radial direction (equivalent to ranging error), and the second term is the uncertainty in the perpendicular

plane (equivalent to bearing estimation error). We define the following scalar variances:

$$\sigma_\rho^2 = \epsilon^2 \sigma_\alpha^2 + \sigma_C^2 \tag{3.11}$$

$$\sigma_u^2 = \sigma_\theta^2 \rho^2 + \sigma_C^2 \tag{3.12}$$

Eqn. 3.11 and Eqn. 3.12 show how the magnitude of the uncertainty in both of the aforementioned directions is obtained. σ_C is a factor that accounts for randomized error as a result of a process to account for the difference between the visual center of the Moon and the gravitational center of the Moon (its value for this study is notated in Table 4.1). This is necessary because this method determines the visual center of the Moon, whereas our dynamics model is relative to the gravitational center of the Moon. ρ is the distance between the satellite and the Moon.

$$\epsilon = \frac{d}{d\alpha}\left[\frac{R_{\text{moon}}}{\sin\alpha}\right] = -R_{\text{moon}}\frac{\cos\alpha}{\sin^2\alpha} \tag{3.13}$$

Eqn. 3.13 is the definition of ϵ. R_{moon} is the radius of the Moon (notated in Table 4.1), and α is the angle between the center of the Moon and edge of the Moon in the lens of the camera. An illustration of what an ellipse representing the outline of the Moon being fitted over a pixilated image of the Moon is shown in Fig. 3.5.

$$P_{cc} = \frac{\partial \vec{c}}{\partial \vec{a}} P_{aa} \frac{\partial \vec{c}}{\partial \vec{a}}^T \tag{3.14}$$

$$P_{cc} \approx \begin{bmatrix} \sigma_\theta^2 & \\ & \sigma_\theta^2 \end{bmatrix} \tag{3.15}$$

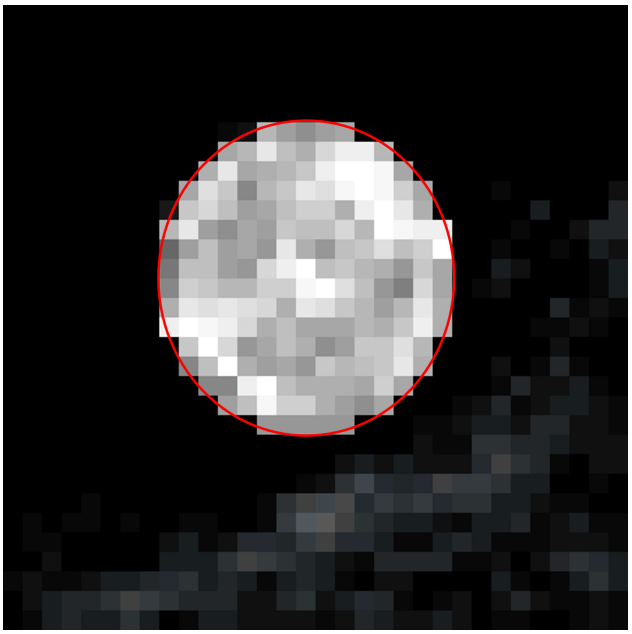

Figure 3.5: Illustration of an ellipse (shown in red) being fitted around a pixelated Moon

To find σ_θ to use in Eqn. 3.12, we first must calculate P_{cc} using Eqn. 3.14.

$$\vec{c} = \begin{bmatrix} x_c \\ y_c \end{bmatrix} \tag{3.16}$$

$$\vec{a} = \begin{bmatrix} A \\ B \\ C \\ D \\ F \\ G \end{bmatrix} = \begin{bmatrix} 1 \\ 0 \\ 1 \\ -2x_c \\ -2y_c \\ x_c^2 + y_c^2 - \alpha^2 \end{bmatrix} \tag{3.17}$$

$\vec{c}$ is the angular coordinates from the center of the photo frame to the center of the Moon. The $\vec{a}$ are the coefficients of the ellipse of the Moon, which we assume to just be a circle

(hence the second equality in Eqn. 3.17). It is for this reason that we can define $\vec{a}$ as we do.

$$P_{aa} = \sigma_{d_i}^2 (H_{LS}^T H_{LS})^{-1} \tag{3.18}$$

P_{aa} is computed according to Eqn. 3.18 for use in Eqn. 3.14.

$$\sigma_\alpha^2 = \frac{\partial \alpha}{\partial \vec{a}} P_{aa} \frac{\partial \alpha}{\partial \vec{a}}^T \tag{3.19}$$

Using Eqn. 3.19, we can also find σ_α.

$$\sigma_{d_i}^2 = \frac{\partial d_i}{\partial \vec{y_i}} R_{yy_i} \frac{\partial d_i}{\partial \vec{y_i}}^T \tag{3.20}$$

$$R_{yy_i} = \sigma_F^2 I_{2x2} \tag{3.21}$$

$$\sigma_F = \frac{\theta_{\text{FOV}}}{n_{\text{pixels}}} \tag{3.22}$$

Finally, we can find σ_{d_i} using Eqn. 3.20 where $\frac{\partial d_i}{\partial \vec{y_i}}$ and H_{LS} are obtained according to Eqn. 3.23 and Eqn. 3.24, respectively. Please note that θ_{FOV} and n_{pixels} are constant values notated in Table 4.1. Note that by calculating σ_F to the precision of a pixel, we are able to find the center of the Moon to a level of precision that is less than a pixel.

$$\frac{\partial d_i}{\partial \vec{y_i}} = \begin{bmatrix} 2Ax_i + By_i + D & Bx_i + 2Cy_i + F \end{bmatrix} \tag{3.23}$$

$$H_{LS} = \begin{bmatrix} \vdots & \vdots & \vdots & \vdots & \vdots \\ \vdots & \vdots & \vdots & \vdots & \vdots \\ x_i^2 & x_i y_i & y_i^2 & x_i & y_i \\ \vdots & \vdots & \vdots & \vdots & \vdots \\ \vdots & \vdots & \vdots & \vdots & \vdots \end{bmatrix} \tag{3.24}$$

$\{(x_1, y_1), ..., (x_n, y_n)\}$ is a set of coordinates on the edge of the Moon within the frame of the camera (i.e., they would be on the red circle shown in Fig. 3.5). We chose the number of points used at each sample time according to Eqn. 3.25.

$$N_{\text{samples}} = \text{floor}\left(2\pi\frac{\alpha_i}{\sigma_F}\right) \tag{3.25}$$

As a note, we also did consider the effect that light diffraction would have on this method's uncertainty, but its effect was negligible when compared to the uncertainty caused by pixilation of the image. Because both of these uncertainties were operationalized in the same way, the effect of diffraction was ignored.

3.1.3 Lunar Mirror Method

Here, we will introduce the lunar mirror method, then cover how we simulated our true measurements for this method, then show how we derived this method's uncertainty model.

Method Introduction

On the Moon, there are several Laser Ranging RetroReflectors (LRRRs, called "lunar mirrors" henceforth). Table 3.1 is a table of 5 of these LRRRs, along with the mission that installed it, and its location [35]. These five mirrors are the ones that were used in this study. To see a diagram of an LRRR, see Fig. 2.5.

At any time that one of these LRRR is within sight of an orbiting satellite, the geometry can be represented by Fig. 3.6.

Importantly, we define an object as being within sight if the satellite was at a positive elevation angle from the perspective of the object. A higher elevation angle restriction for

Mission	Installation Date	Latitude	Longitude
Apollo 11	July 21st, 1969	0.6734° N	23.4731° E
Luna 17	November 17th, 1970	38.3152° N	35.0080° W
Apollo 14	January 31st, 1971	3.6442° S	17.4786° W
Apollo 15	July 31st, 1971	26.1334° N	3.6285° E
Luna 21	January 15th, 1973	25.8323° N	30.9221° E

Table 3.1: Lunar Mirror Locations [35]

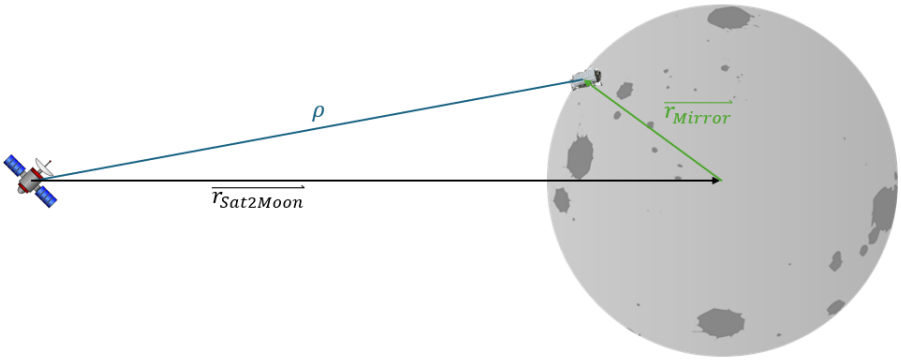

Figure 3.6: Lunar Mirror Measurement Diagram

the LRRRs specifically would be more realistic, but we wanted an optimistic picture of the capability of the lunar mirror method.

Suppose that we had a laser-ranging system on our satellite, and we could find out how far away a given LRRR is from our satellite. We could simulate that measurement with Eqn. 3.26.

$$\rho = ||\vec{r}_{\text{sat2moon}} + \vec{r}_{\text{mirror}}||_2 \tag{3.26}$$

By comparing the actual measurement with our simulated measurement (i.e., comparing ρ calculated using Eqn. 3.26 to our measurement gathered from our laser-ranging system), we could improve our estimate of our satellite's state. This modeling of the measurement from the laser-ranging system is idealized and time-of-flight-based two-way ranging equations would be a more accurate way to simulate it, but this captures the geometry of the observations sufficiently enough for this study.

True Measurement Simulation

For obtaining the true measurements for the lunar mirror measurement method, access was computed from the satellite to the five mirrors identified in Table 3.1 for each of the six orbits using STK. The vector from the satellite to each mirror at each sample time when a line of sight vector could be established was recorded. Once these vectors were recorded, their magnitudes were calculated and used as the measurements.

Uncertainty Model

The moment our satellite-mounted laser-ranging system (LRS) produces a range measurement can be illustrated as in Fig. 3.6. For information on the assumed specifications for our LRS, please refer to section 4.1.2. The travel time of the light from the LRS to produce our measurement can be related to our measurement using Eqn. 3.27 from [16] where c is the speed of light (notated in Table 4.1), ρ is the measured distance from the satellite to the mirror, and t_{flight} is the two-way travel time of the laser pulse. We also assume that the returning light from the LRS is always observable, meaning we ignore unfavorable lighting conditions on the surface of the Moon

$$t_{\text{flight}} = \frac{2\rho}{c} \tag{3.27}$$

For our idealized measurement model, any radial movement while the laser pulse from the LRS is en route will result in measurement error. We can multiply the travel time of the light by the magnitude of our velocity at the time of measurement to simulate a worst-case scenario for measurement error caused by satellite movement. This uncertainty (called σ_m) is calculated for every measurement, squared, then added to the squared error inherent in the LRS (called σ_L, which is notated in Table 4.1). This process is recapped in Eqns. 3.28

and 3.29

$$\sigma_{m_i} = t_{\text{flight}_\rangle} \|\vec{v_i}\|_2 \tag{3.28}$$

$$R_i = \sigma_{m_i}^2 + \sigma_L^2 \tag{3.29}$$

3.2 Propagation of the Truth Reference Orbits

In this section, we will cover how we used STK to simulate the true state information for each of our test orbits, what dynamics model we used in this study, and how we used quaternions to convert between the International Celestial Reference Frame (ICRF) and Earth-Moon synodic frame.

3.2.1 STK Truth Simulation

Within STK, we first constructed a new central body to represent the Moon in a circular orbit. We then created a new propagator that only accounted for circular restricted three-body problem (CR3BP) dynamics between Earth and our newly-defined central body. We assume that the Earth and Moon are point masses, that there are no other sources of gravity, and that both the Earth and Moon are perfectly spherical. These dynamics are covered in section 3.2.2. This relatively simplistic model was chosen because this study is more focused on comparing our three chosen methods to one another, and less focused on simulating how these methods would perform in reality with a very high degree of accuracy. The forces we neglected, such as radiation pressures, tidal forces, and non-point mass gravity deviations are not expected to change the performance of any method significantly, and would have even less of an effect on conclusions drawn by comparing the methods' accuracy results to

one another.

We obtained initial conditions for our test cases from the JPL CR3BP periodic orbit database [7]. A satellite representing each test case was then added to our STK scenario and given our chosen initial conditions.

We used newly-defined CR3BP propagator and the "RKF7th8th" integrator (tolerance for the integrator was 1×10^{-13} km) to propagate each of the test orbits for 30 days. The differential corrector tool was used to adjust our initial conditions if a particular satellite drifted off of the chosen halo orbit path before 30 days had elapsed (This was necessary to correct for any slight modeling/integration differences between STK's model and the original JPL database.).

Finally, we sampled the state vector and quaternions that described the rotation between the ICRF frame and Earth-Moon synodic every second for each satellite over the 30-day interval. The ICRF frame is an inertial frame that is defined in [14]. The Earth-Moon synodic frame is a rotating coordinate system that is defined with the x axis pointing from the Earth to the Moon, and the z axis is perpendicular to the Moon's orbital plane as well as co-direction to the Moon's angular momentum vector. Implementing conversions between these two frames using these two quaternions was necessary because the dynamics model equations were only valid in the synodic frame, whereas the measurement methods were evaluated in the ICRF frame.

3.2.2 Circular Restricted Three-Body Problem Equations

In this study, we use the standard process for finding our acceleration in the synodic frame. We begin with normalizing our satellite's position and velocity within the synodic frame as shown in Eqns. 3.30 and 3.31, as depicted in [2]. The value for $d_{\text{earth2moon}}$ is notated in Table

4.1. To clarify, the normalized values have no bar above them.

$$\begin{bmatrix} x \\ y \\ z \end{bmatrix} = \frac{1}{d_{\text{earth2moon}}} \begin{bmatrix} \bar{x} \\ \bar{y} \\ \bar{z} \end{bmatrix} \tag{3.30}$$

$$\begin{bmatrix} \dot{x} \\ \dot{y} \\ \dot{z} \end{bmatrix} = \frac{1}{\sqrt{\frac{\mu_{\text{moon}}+\mu_{\text{earth}}}{d_{\text{earth2moon}}}}} \begin{bmatrix} \bar{\dot{x}} \\ \bar{\dot{y}} \\ \bar{\dot{z}} \end{bmatrix} \tag{3.31}$$

To simplify our equations, we calculate μ as shown in Eqn. 3.32. The values for μ_{moon} and μ_{earth} are notated in Table 4.1.

$$\mu = \frac{\mu_{\text{moon}}}{\mu_{\text{moon}} + \mu_{\text{earth}}} \tag{3.32}$$

Before we can calculate our normalized acceleration within the synodic frame, we must calculate ρ_1 and ρ_2 using Eqns. 3.33 and 3.34. This follows the process outlined in [2].

$$\rho_1 = \sqrt{(x+\mu)^2 + y^2 + z^2} \tag{3.33}$$

$$\rho_2 = \sqrt{(x+\mu-1)^2 + y^2 + z^2} \tag{3.34}$$

We find our normalized synodic frame acceleration according to Eqns. 3.35–3.37 [2].

$$\ddot{x} = x + 2\dot{y} - \frac{1-\mu}{\rho_1^3}(x+\mu) - \frac{\mu}{\rho_2^3}(x+\mu-1) \tag{3.35}$$

$$\ddot{y} = y - 2\dot{x} - \left(\frac{1-\mu}{\rho_1^3} + \frac{\mu}{\rho_2^3}\right) y \tag{3.36}$$

$$\ddot{z} = -\left(\frac{1-\mu}{\rho_1^3} + \frac{\mu}{\rho_2^3}\right) z \tag{3.37}$$

Then, we convert our acceleration back into dimensional units as shown in Eqn. 3.38.

$$\begin{bmatrix} \ddot{\bar{x}} \\ \ddot{\bar{y}} \\ \ddot{\bar{z}} \end{bmatrix} = \begin{bmatrix} \ddot{x} \\ \ddot{y} \\ \ddot{z} \end{bmatrix} \frac{\mu}{d^2_{\text{earth2moon}}} \tag{3.38}$$

Our only deviation from the standard process is shown in Eqn. 3.39. We add a perturbation vector based on our process noise covariance as our final step ($\vec{\mathcal{E}}_{vk}$ is defined in Eqn. 3.44):

$$\begin{bmatrix} \dot{\bar{x}} \\ \dot{\bar{y}} \\ \dot{\bar{z}} \\ \ddot{\bar{x}} \\ \ddot{\bar{y}} \\ \ddot{\bar{z}} \end{bmatrix} = \begin{bmatrix} \dot{\bar{x}} \\ \dot{\bar{y}} \\ \dot{\bar{z}} \\ \ddot{\bar{x}} \\ \ddot{\bar{y}} \\ \ddot{\bar{z}} \end{bmatrix} + \vec{\mathcal{E}}_{vk} \tag{3.39}$$

Note that we only add this process noise vector when performing state propagation inside of our filter, not when simulating our true state measurements with STK. This was done because it would be unrealistic if our filter's dynamics model perfectly matched, as in practice there are always accelerations that cannot be predicted by even the most accurate of dynamics models, but these perturbations would cause our satellites to depart from their respective halo orbits if we added these perturbations to the STK's dynamics model. Therefore, we add noise to our filter's state propagation to equivalently inject realistic uncertainty without needing to implement a controller to maintain our halo orbits in the truth simulations.

3.2.3 Coordinate Conversions via Quaternions

As covered in section 3.2.1, we collected quaternions that described the rotation between the ICRF frame and synodic frame once per second for each test case's entire 30-day test interval. Our collected true state data was in the ICRF frame, and our measurement models also operated in the ICRF frame, but our dynamics model equations (section 3.2.2) were only applicable in the synodic frame. This is why these quaternions were necessary.

For dynamic propagation within our UKF, we would rotate our state vector at time k into the synodic frame using the quaternions applicable at k, propagate it using MATLAB's `ode113.m` (with an absolute and relative tolerance of 1×10^{-13} km) and our dynamics model, then rotate them back into the ICRF frame using the applicable quaternions at time $k+1$. This was done to maintain future extensibility to more general frame definitions, the elliptical-restricted equations of motion, or other higher-fidelity analytic models while maintaining the ability to directly incorporate inertial measurements (e.g. star positions).

It was also found that our quaternions were not numerically accurate enough to provide smooth frame conversions to the required precision with the specified time step, so we applied a Savitsky-Golay filter [33] via MATLAB's `sgolayfilt.m` function to smooth out our quaternions.

3.3 Unscented Kalman Filter

In this section, we will cover the implementation of the augmented unscented Kalman filter (UKF) we used in this study. This particular implementation uses augmented sigma points for process noise, but implicitly accounts for measurement noise through an analytical approach. This closely follows the formulation described in [29].

We begin by computing the Cholesky factors of the process noise covariance and state covariance as shown in Eqns. 3.41 and 3.40 respectively:

$$S_{x_k} S_{x_k}^T = P_k \tag{3.40}$$

$$S_{v_k} S_{x_k}^T = Q_k \tag{3.41}$$

From these Cholesky factors, we split up their columns as shown in Eqns. 3.42 and 3.43. Please note that n_x is the number of state variables (six for this study) and n_v is the number of process noise variables (also six for this study).

$$S_{x_k} = \begin{bmatrix} \vec{s}_{x1k} & \vec{s}_{x2k} & \dots & \vec{s}_{xn_xk} \end{bmatrix} \tag{3.42}$$

$$S_{v_k} = \begin{bmatrix} \vec{s}_{v1k} & \vec{s}_{v2k} & \dots & \vec{s}_{vn_vk} \end{bmatrix} \tag{3.43}$$

We then define our random acceleration perturbation vector as shown in Eqn. 3.44.

$$\vec{\mathcal{E}}_{vk} = S_{v_k} \begin{bmatrix} 0_{3\times1} \\ \nu_k \end{bmatrix}, \quad \nu_k \sim \mathcal{N}(0_{3\times1}, I_{3\times3}) \tag{3.44}$$

We generate $1 + 2(n_x + n_v)$ sigma points at sample k in $\begin{bmatrix} \vec{x}(k) \\ \vec{v}(k) \end{bmatrix}$ space. Let i be the sigma point index that ranges from $0, ..., 2(n_x + n_v)$. The formulae for defining our sigma points

are shown in Eqns. 3.45–3.54:

$$\vec{\mathcal{X}}^i_{k|k} = \vec{x}_{k|k} \quad \text{for} \quad i = 0 \tag{3.45}$$

$$\vec{\mathcal{V}}^i_k = 0_{n_v \text{x} 1} \quad \text{for} \quad i = 0 \tag{3.46}$$

$$\vec{\mathcal{X}}^i_{k|k} = \vec{x}_{k|k} + \sqrt{(n_x + n_v + \lambda)}\vec{s}_{xik} \quad \text{for} \quad i = 1, ..., n_x \tag{3.47}$$

$$\vec{\mathcal{V}}^i_k = 0_{n_v \text{x} 1} \quad \text{for} \quad i = 1, ..., n_x \tag{3.48}$$

$$\vec{\mathcal{X}}^i_{k|k} = \vec{x}_{k|k} - \sqrt{(n_x + n_v + \lambda)}\vec{s}_{x(i-n_x)k} \quad \text{for} \quad i = (n_x + 1), ..., (2n_x) \tag{3.49}$$

$$\vec{\mathcal{V}}^i_k = 0_{n_v \text{x} 1} \quad \text{for} \quad i = (n_x + 1), ..., (2n_x) \tag{3.50}$$

$$\vec{\mathcal{X}}^i_{k|k} = \vec{x}_{k|k} \quad \text{for} \quad i = (2n_x + 1), ..., (2n_x + n_v) \tag{3.51}$$

$$\vec{\mathcal{V}}^i_k = \sqrt{(n_x + n_v + \lambda)}\vec{s}_{v(i-2n_x)k} \quad \text{for} \quad i = (2n_x + 1), ..., (2n_x + n_v) \tag{3.52}$$

$$\vec{\mathcal{X}}^i_{k|k} = \vec{x}_{k|k} \quad \text{for} \quad i = (2n_x + n_v + 1), ..., (2n_x + 2n_v) \tag{3.53}$$

$$\vec{\mathcal{V}}^i_k = -\sqrt{(n_x + n_v + \lambda)}\vec{s}_{v(i-2n_x-n_v)k} \quad \text{for} \quad i = (2n_x + n_v + 1), ..., (2n_x + 2n_v) \tag{3.54}$$

We also add our random acceleration perturbation vector defined in Eqn. 3.44 to our process noise sigma points as shown in Eqn. 3.55.

$$\vec{\mathcal{V}}^i_k = \vec{\mathcal{V}}^i_k + \vec{\mathcal{E}}_{vk} \tag{3.55}$$

λ (defined in Eqn. 3.56) is an important constant that is a function of our tuning parameter values. The values used for α_p and κ_p can be found in Table 4.1.

$$\lambda = \alpha_p^2(n_x + n_v + \kappa_p) - (n_x + n_v) \tag{3.56}$$

Now we perform dynamic propagation of our sigma points. Eqn. 3.57 describes using our dynamics model to numerically integrate to our new time step, and Eqn. 3.58 describes using our selected measurement method to simulate our measurement at our new sample

time a priori. Please note that $\vec{p}_k$ is a parameter vector for constants that are required for propagation, which can change depending on your specific dynamics model. For the dynamics model used in this study, refer to section 3.2.2. Note that when i is used in a superscript, it denotes an index.

$$\vec{\mathcal{X}}^i_{k+1|k} = \boldsymbol{f}[k, \vec{\mathcal{X}}^i_{k|k}, \vec{p}_k, \vec{\mathcal{V}}^i_k] \quad \text{for} \quad i = 0, ..., (2n_x + 2n_v) \tag{3.57}$$

$$\vec{\mathcal{M}}^i_{k+1} = \boldsymbol{h}[k+1, \vec{\mathcal{X}}^i_{k+1|k}, \vec{p}_k] \quad \text{for} \quad i = 0, ..., (2n_x + 2n_v) \tag{3.58}$$

With dynamic propagation complete, we can now calculate our a priori state and measurement vectors according to Eqns. 3.59 and 3.60 respectively.

$$\vec{x}_{k+1|k} = \sum_{i=0}^{2(n_x+n_v)} W_i^{(m)} \vec{\mathcal{X}}^i_{k+1|k} \tag{3.59}$$

$$\vec{z}_{k+1|k} = \sum_{i=0}^{2(n_x+n_v)} W_i^{(m)} \vec{\mathcal{M}}^i_{k+1} \tag{3.60}$$

Please note that $W_i^{(m)}$ is calculated according to Eqns. 3.61 and 3.62. The superscript (m) stands for "mean" and is not an index.

$$W_i^{(m)} = \frac{\lambda}{n_x + n_v + \lambda} \quad \text{for} \quad i = 0 \tag{3.61}$$

$$W_i^{(m)} = \frac{1}{2(n_x + n_v + \lambda)} \quad \text{for} \quad i = 1, ..., (2n_x + 2n_v) \tag{3.62}$$

Now we can calculate our a priori covariance matrices according to Eqns. 3.63–3.65. $W_i^{(c)}$ is calculated according to Eqns. 3.66 and 3.67. The value used for β_p in this study is notated

in Table 4.1.

$$P_{k+1|k} = \sum_{i=0}^{2(n_x+n_v)} W_i^{(c)} \left[\vec{\mathcal{X}}_{k+1|k}^i - \vec{x}_{k+1|k}\right] \left[\vec{\mathcal{X}}_{k+1|k}^i - \vec{x}_{k+1|k}\right]^T \tag{3.63}$$

$$P_{xz,k+1|k} = \sum_{i=0}^{2(n_x+n_v)} W_i^{(c)} \left[\vec{\mathcal{X}}_{k+1|k}^i - \vec{x}_{k+1|k}\right] \left[\vec{\mathcal{M}}_{k+1}^i - \vec{z}_{k+1|k}\right]^T \tag{3.64}$$

$$P_{zz,k+1|k} = R_{k+1} \sum_{i=0}^{2(n_x+n_v)} W_i^{(c)} \left[\vec{\mathcal{M}}_{k+1}^i - \vec{z}_{k+1|k}\right] \left[\vec{\mathcal{M}}_{k+1}^i - \vec{z}_{k+1|k}\right]^T \tag{3.65}$$

$$W_i^{(c)} = \frac{\lambda}{n_x + n_v + \lambda} + 1 - \alpha_p^2 + \beta_p \quad \text{for} \quad i = 0 \tag{3.66}$$

$$W_i^{(c)} = \frac{1}{2(n_x + n_v + \lambda)} \quad \text{for} \quad i = 1, ..., (2n_x + 2n_v) \tag{3.67}$$

Now we calculate the Cholesky factor of our measurement covariance matrix according to Eqn. 3.68. Then we calculate our measurement perturbation vector using Eqn. 3.69, before adding it to our true measurement vector as described in Eqn. 3.70.

$$S_{z_{k+1}} S_{z_{k+1}}^T = R_{k+1} \tag{3.68}$$

$$\vec{\mathcal{E}}_{zk+1} = S_{z_{k+1}} \nu_z, \quad \nu_z \sim \mathcal{N}(0_{n_z \times 1}, I_{n_z \times n_z}) \tag{3.69}$$

$$\vec{z}_{k+1} = \vec{z}_{k+1} + \vec{\mathcal{E}}_{zk+1} \tag{3.70}$$

Then we conduct a χ^2 test on the measurement residuals to reject any improperly-processed or high-noise measurements. We calculate χ^2 according to Eqn. 3.71. If χ^2 was greater than eight, we rejected the measurement, we did not include any innovation or covariance update from this measurement.

$$\chi^2 = \left[\vec{z}_{k+1} - \vec{z}_{k+1|k}\right]^T P_{zz_{k+1|k}}^{-1} \left[\vec{z}_{k+1} - \vec{z}_{k+1|k}\right] \tag{3.71}$$

Finally, we calculate our a posteriori state vector and state covariance according to Eqns. 3.72 and 3.73 respectively.

$$\vec{x}_{k+1|k+1} = \vec{x}_{k+1|k} + P_{xz_{k+1|k}} P^{-1}_{zz_{k+1|k}} \left[\vec{z}_{k+1} - \vec{z}_{k+1|k}\right] \tag{3.72}$$

$$P_{k+1|k+1} = P_{k+1|k} - P_{xz_{k+1|k}} P^{-1}_{zz_{k+1|k}} P^{T}_{xz_{k+1|k}} \tag{3.73}$$

We selected a UKF for this study to avoid the added complexity of needing to explicitly calculate derivatives for each of our methods.

Chapter 4

Results and Discussion

In this chapter, we will briefly discuss our test case orbits and parameters once again before discussing the results of our performance evaluations for these methods. We will discuss the strengths and weaknesses of each method, as well as postulate on some effects that may have not been captured by our testing. It should be noted that all tabulated errors were calculated after "convergence" for each test, which means that data that occurred before the predicted error magnitude reached its median value for the first time was not used in error calculations. This was done to compare the methods to one another after they've begun to function optimally, but the eliminated data can still be seen on graphs of the results. It should be noted that it was possible to define that the error had converged in this way because our error was periodic. This would no longer be true if lighting conditions were accounted for.

4.1 Test Conditions

In this section, we will be discussing the test conditions used to collect our results. We first will walk through the initial conditions used for each of our test case orbits, as well as discuss how these orbits were chosen. Then we will discuss the specifications of our chosen sensors that we used to make our uncertainty models more realistic. Finally, we will show every mathematical constant used in this study.

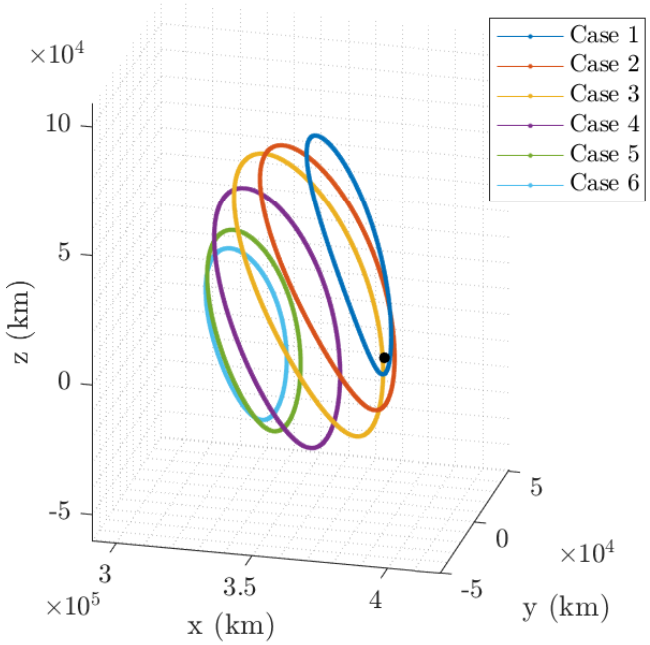

Figure 4.1: All test cases, shown in the synodic frame with the Moon for scale

4.1.1 Orbits Tested

In Fig. 4.1, we can see the orbits used for testing in this study; all are Earth-Moon L_1 northern halo orbits. Their identifiers (Case 1, Case 2, etc.) will be used to refer to them during the presentation of the results for each method. For all orbits, their initial conditions were a point at the top of their trajectories (i.e., the point at where the z coordinate was at its maximum), and they were propagated for 30 days from this initial point. We chose to use exclusively halo orbits because they are widely used for scientific discovery. We also chose to specifically use halo orbits in the L_1 family because the LRRRs are only on the Earth-facing side of the Moon. The initial conditions were chosen from [7].

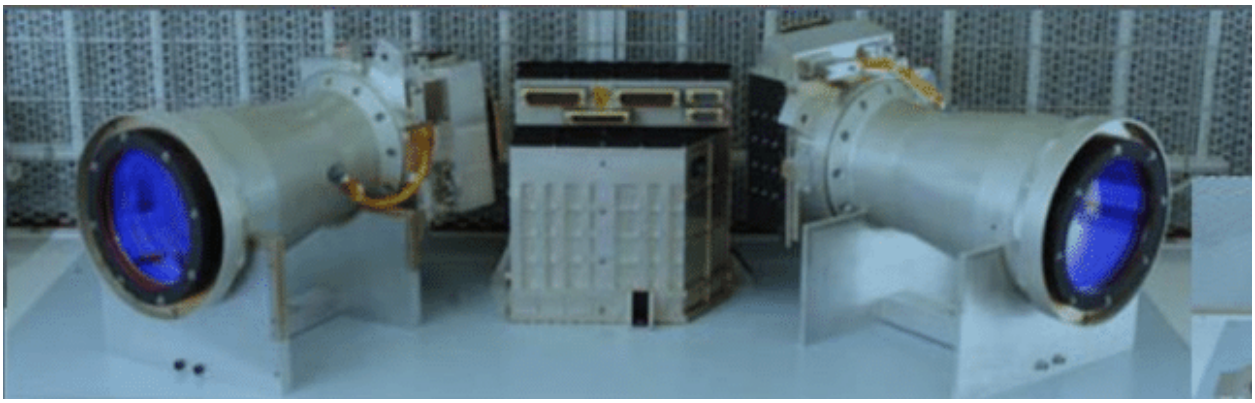

Figure 4.2: Ball HAST Sensor Heads (Figure reproduced from [12])

4.1.2 Hardware Used

To make our uncertainty models more realistic, we incorporated specifications from the Ball Aerospace High Accuracy Star Tracker (HAST) when possible. The full specifications of the HAST can be found here [25].

The HAST contains two sensor heads for added reliability and accuracy (see Fig. 4.2), but the specifications of only one were used for our uncertainty models to make our error estimates more conservative. Each sensor head has a field of view of 8.8 × 8.8 degrees. The camera in each sensor head is also 2048 pixels × 2048 pixels.

We also assumed that the HAST was operating on default settings. This means it could only detect stars brighter than a visual magnitude of 5.5, and took pictures at a frame rate of 55 Hz.

Note that an LRS would be required for the lunar mirror method to function, but this system would likely need to be bespoke, so a real product was not used for testing. For the assumed error of our LRS, we used the value that was used in [38].

It also should be noted that other than filtering out occultations with stars that would be too dim to be detected by the HAST, this study ignored all other lighting constraints (e.g., we

Constant	Value
σ_{terrain}	1×10^{-2} km
t_{frame}	0.0179 s
L_{min}	5.5 Magnitude
R_{moon}	1737.4 km
Δt	1×10^{-6} s
σ_C	0.2 km
θ_{FOV}	8.8°
n_{pixels}	2048 pixels
c	2.9979×10^5 km/s
σ_L	0.5996 km
$d_{\text{earth2moon}}$	390 877.4158 km
μ_{moon}	4902.8003 km^3/s^2
μ_{earth}	398 600.4418 km^3/s^2
α_p	1
κ_p	-9
β_p	2

Table 4.1: Constants Table

assumed all mirrors were illuminated, all occultations occurred on the darkened side of the Moon, and the entire Moon was illuminated for optical ranging measurements). This was done to compare how these methods would function in ideal circumstances to one another.

4.1.3 Test Parameters

Table 4.1 contains the implemented values of all the mathematical constants used in our study.

4.2 Navigation Accuracy Test Results

In this section, we will discuss the accuracy results for each method. Each subsection will be dedicated to one of the methods, where we will cover its data-driven strengths and weaknesses

Star Occultation Method Results							
		Case 1	Case 2	Case 3	Case 4	Case 5	Case 6
Error (Centile)	Pos. 10% (km)	9.07×10^{-3}	8.48×10^{-3}	1.12×10^{-2}	1.37×10^{-2}	2.32×10^{-2}	1.48×10^{-2}
	Pos. 50% (km)	1.30×10^{-1}	7.37×10^{-2}	5.60×10^{-2}	8.02×10^{-2}	7.64×10^{-2}	5.93×10^{-2}
	Pos. 90% (km)	2.68×10^{-1}	2.19×10^{-1}	1.66×10^{-1}	1.56×10^{-1}	2.48×10^{-1}	3.13×10^{-1}
	Vel. 10% (km/s)	3.20×10^{-7}	2.70×10^{-7}	2.76×10^{-7}	2.76×10^{-7}	3.29×10^{-7}	2.48×10^{-7}
	Vel. 50% (km/s)	8.82×10^{-7}	5.82×10^{-7}	6.17×10^{-7}	5.52×10^{-7}	7.61×10^{-7}	6.07×10^{-7}
	Vel. 90% (km/s)	1.52×10^{-6}	1.13×10^{-6}	1.13×10^{-6}	9.55×10^{-7}	1.94×10^{-6}	1.97×10^{-6}
# of Occultations		3704	909	609	366	268	217
Perilune (km)		5.58×10^{3}	1.79×10^{4}	2.79×10^{4}	3.95×10^{4}	4.56×10^{4}	4.74×10^{4}
Apolune (km)		8.67×10^{4}	8.68×10^{4}	8.75×10^{4}	8.15×10^{4}	7.39×10^{4}	7.11×10^{4}
# of Revolutions		3.72	3.09	2.69	2.44	2.42	2.43

Table 4.2: Summary of results for the star occultation method

as compared to the other methods. For clarity, we will not show the detailed results from every conducted test, but these can be seen in Appendix A.

4.2.1 Star Occultation Method

To easily compare the performance of this method across the six test cases, Table 4.2 is provided. Similar tables will be provided in other sections for the other methods. The 10th-percentile, 50th-percentile, and 90th-percentile errors for both the position and velocity make up the first six rows. These values are calculated after convergence is achieved, meaning that the filter only performed with lower error values than the 10th-percentile metrics at ten percent of our sample times after steady-state was achieved (the 50th-percentile and 90th-percentile metrics function similarly). This means that the 10th-percentile metric represents how well the filter operated using this method under ideal circumstances, whereas the 90th-percentile metrics represent a sensible error bound for that method's performance in that test case. A low disparity between the 10th-percentile and 90th-percentile error metrics represent stable performance for that method in that particular test case, and a high disparity conversely represents a more erratic performance. Other metrics displayed in the table can help us to understand why a given method may have performed better on certain

test cases than others, such as the star occultation method tending to perform better on cases where more occultations are observed.

As can be seen in Table 4.2, the star occultation method functioned the best on the test cases that passed the closest to the Moon (Case 1 has the lowest perilune distance, Case 6 has the highest perilune distance). This is hardly surprising, as more occultations occur when the Moon occupies a larger region in the field of view of the star cameras. It was noted for all cases that large amounts of occultations occurred when the satellite was near perilune, and then very few occultations occurred outside of this region. Interestingly, while the lowest 10th-percentile (best case) position errors occurred on Cases 1 and 2, which were the two cases that passed the closest to the Moon, they also had the largest variation between the 90th-percentile (worst case) position errors. This suggests that the star occultation method is sensitive to high changes in velocity, or simply does not cope well with how sensitive the dynamics of halo orbits can become when they pass close to the Moon. This is supported by Case 2 having lower errors in every tested metric, despite having less than a quarter of the number of occultations of Case 1. For reference, the results for Case 1 and 2 can be seen in Figs. 4.3 and 4.4 respectively. In each of these figures, the first and third graphs show the position and velocity errors respectively in the x, y, and z directions of the ICRF frame. The second and fourth graphs show the magnitudes of the position and velocity errors respectively. The dashed black lines represent the estimated error bound, while the solid lines represent the true error. In all graphs, the vertical red lines show a time when an occultation occurred, the dotted blue line shows when convergence was achieved, and the green lines represent apolune.

As can be seen in Table 4.2, the 90th-percentile velocity error seems to be very stable from Cases 2–4 (this ignores Case 1, as it was the most unstable), but then seems to jump rapidly in Cases 5–6. This suggests that velocity error is less unstable in orbits with high changes in

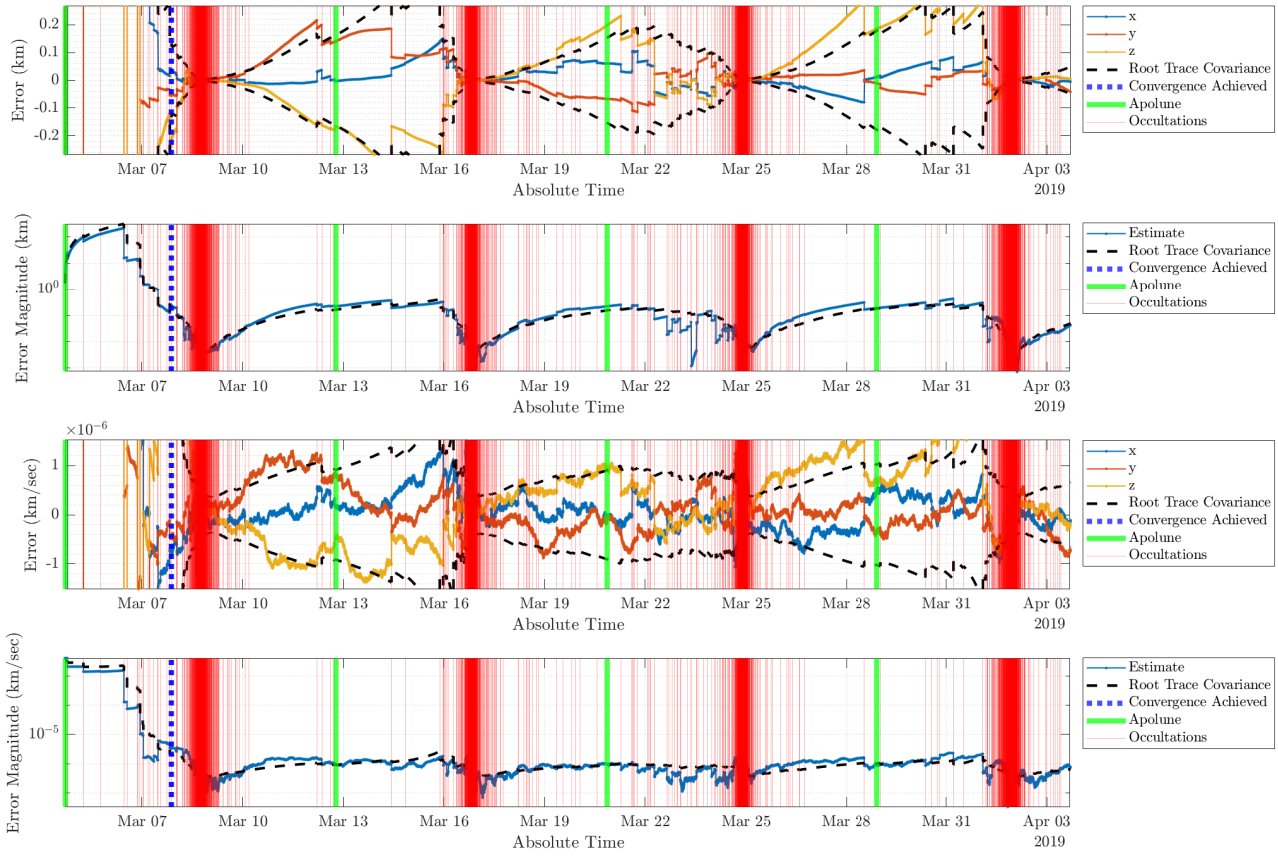

Figure 4.3: Star Occultation Method Results for Case 1. This case had the most observed occultations, but its performance was unstable due to how close this case passed to the Moon.

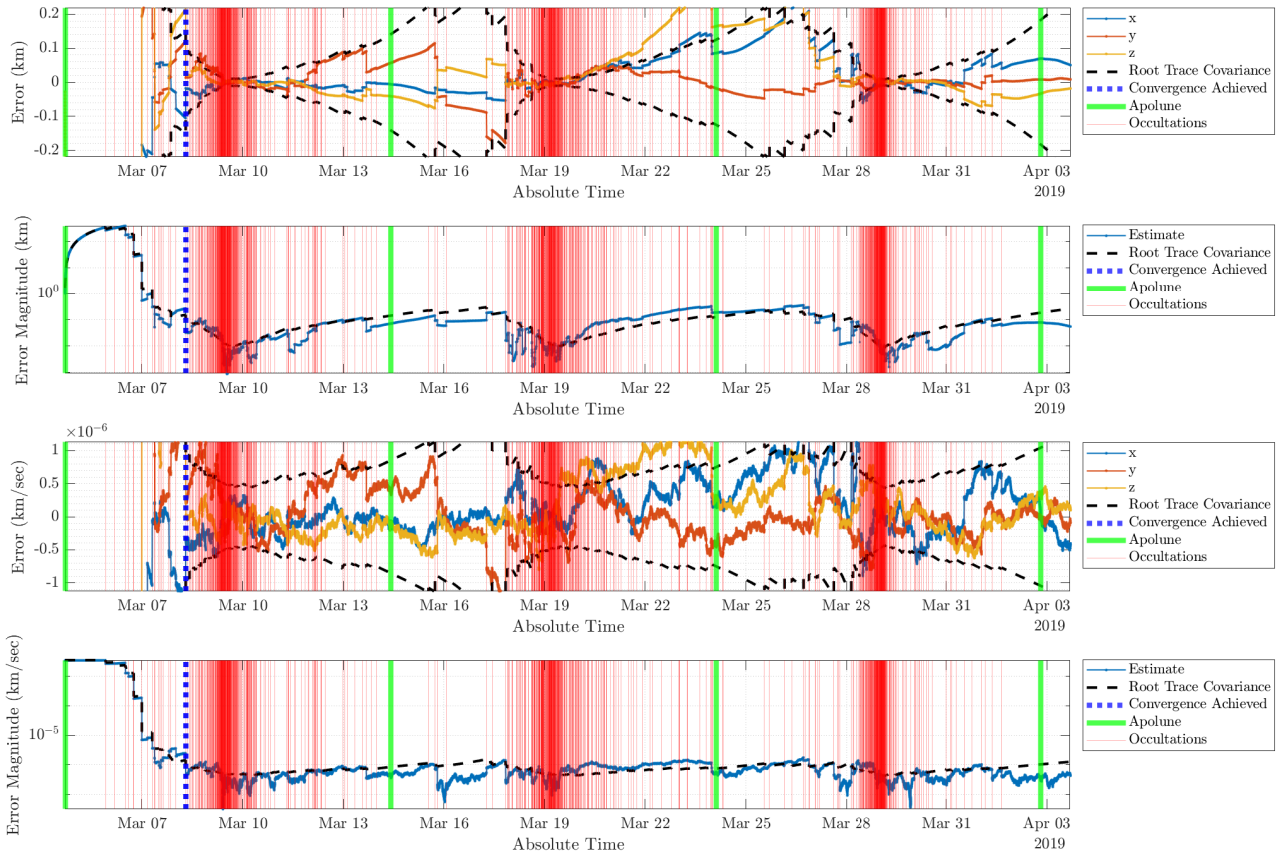

Figure 4.4: Star Occultation Method Results for Case 2. This case performed better than Case 1, despite having less than a quarter of the number of occultations as Case 1.

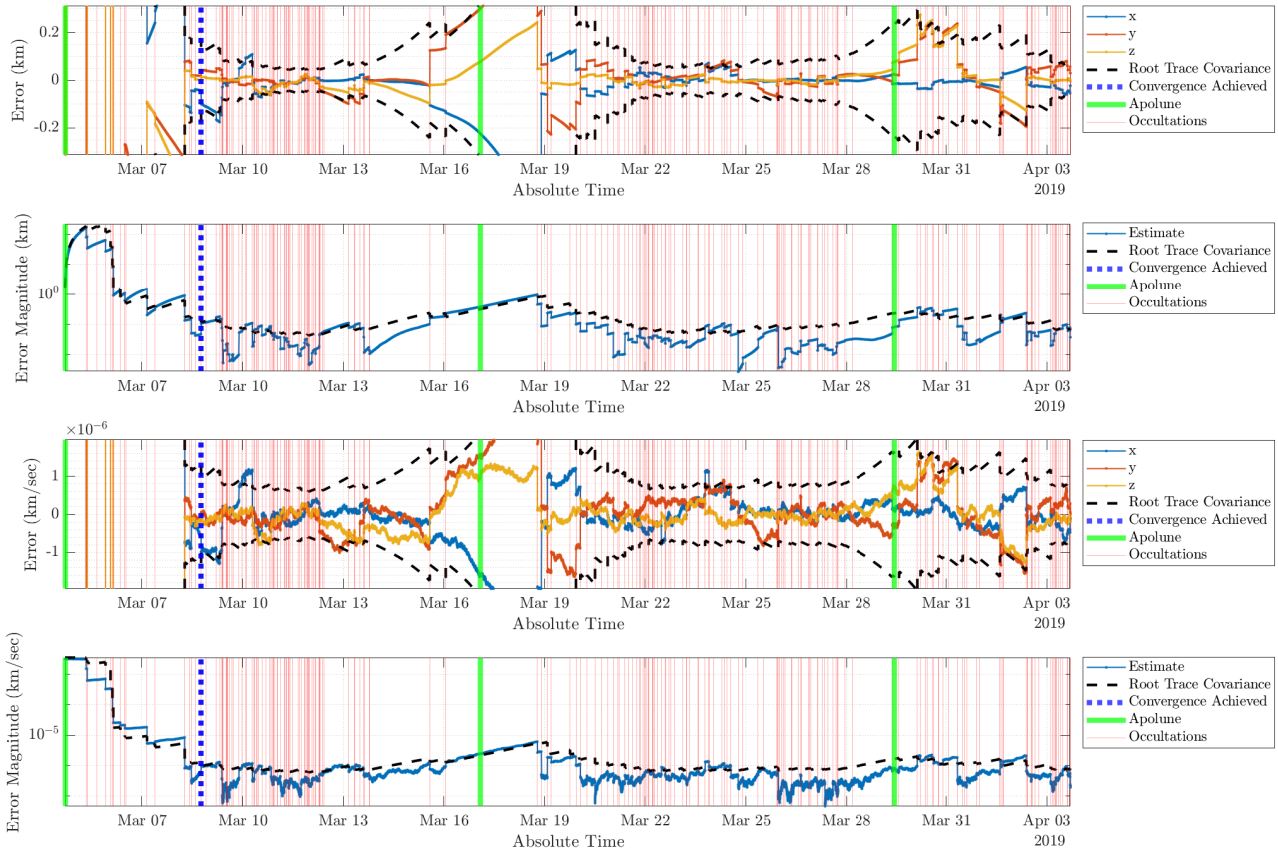

Figure 4.5: Star Occultation Method Results for Case 6. This case had the fewest occultations and the worst 90th-percentile error metrics for both position and velocity, but its performance was not nearly as erratic as Case 1.

velocity and close lunar approaches than position error. For reference, Case 6's results can be seen in Fig. 4.5.

While the star occultation method did not perform better than the optical navigation method for any of our tested cases (as will be shown in section 4.2.2), the same can not be said for the lunar mirror method. The star occultation method had a better 90th-percentile position error and velocity error than the lunar mirror method for Cases 1–4, suggesting overall more reliable performance for these cases than the lunar mirror method. The lunar mirror method

Optical Navigation Method Results							
		Case 1	Case 2	Case 3	Case 4	Case 5	Case 6
Error (Centile)	Pos. 10% (km)	2.27×10^{-3}	1.91×10^{-3}	2.17×10^{-3}	2.05×10^{-3}	2.02×10^{-3}	2.11×10^{-3}
	Pos. 50% (km)	4.68×10^{-3}	3.98×10^{-3}	4.56×10^{-3}	4.33×10^{-3}	4.05×10^{-3}	4.30×10^{-3}
	Pos. 90% (km)	7.64×10^{-3}	7.68×10^{-3}	7.74×10^{-3}	7.00×10^{-3}	6.69×10^{-3}	6.85×10^{-3}
	Vel. 10% (km/s)	1.40×10^{-7}	1.06×10^{-7}	1.30×10^{-7}	1.20×10^{-7}	1.15×10^{-7}	1.20×10^{-7}
	Vel. 50% (km/s)	2.62×10^{-7}	2.29×10^{-7}	2.57×10^{-7}	2.42×10^{-7}	2.35×10^{-7}	2.37×10^{-7}
	Vel. 90% (km/s)	4.43×10^{-7}	4.02×10^{-7}	4.08×10^{-7}	3.92×10^{-7}	3.86×10^{-7}	3.93×10^{-7}
Perilune (km)		5.58×10^{3}	1.79×10^{4}	2.79×10^{4}	3.95×10^{4}	4.56×10^{4}	4.74×10^{4}
Apolune (km)		8.67×10^{4}	8.68×10^{4}	8.75×10^{4}	8.15×10^{4}	7.39×10^{4}	7.11×10^{4}
Blackout per revolution (mins/rev)		1054.97	1017.68	0.00	0.00	0.00	0.00
Total blackout period (mins)		4219.82	3053.02	0.00	0.00	0.00	0.00
# of Revolutions		3.72	3.09	2.69	2.44	2.42	2.43

Table 4.3: Summary of results for the optical navigation method

was better for the cases with the greatest perilune distance (Cases 5 and 6), which is where the star occultation method had the fewest occultation to work with (Table 4.2) and the lunar mirror method had more two or more mirrors visible for the entire testing period (Table 4.4).

Issues with numerical stability were noticed with this method in particular, and a chi-squared test was implemented to reduce this problem. This was particularly a problem with the case that passed the closest to the Moon (Case 1), which suffered from enough instability to cause the filter to fail. It seemed this was caused because the method was most sensitive to measurement errors when the satellite was closest to the Moon, and because of the low amount of measurements compared to the other methods, it was unable to correct itself.

To see the graphs of the cases that were not discussed here, please see Appendix A.1.

4.2.2 Optical Navigation Method

The optical navigation method was the least computationally intensive and most stable of all the tested methods (Note that this was due to our simplifications. If we truly had to process

an image and fit an ellipse each frame, this would absolutely be the most computationally intensive method.). As seen in Table 4.3, its 90th-percentile position error grew as the apolune distance grew, and seemed to not be as affected by the "blackout periods" as the 10th-percentile and 50th-percentile position error. For clarification, a "blackout period" is a period of time where the satellite is too close to the Moon for the entire Moon to fit in the field of view of our star camera (which had a FOV of 8.8 $\times$ 8.8 degrees), thus no measurements for this method can be taken. An example of what a result with blackout periods looks like can be seen in Fig. 4.6, where the blackouts occur where a spike in data can be seen. Note that the layout of all figures in this subsection are similar to the layout of Fig. 4.3.

As can be seen in Table 4.3, the error values of Case 2 are lower than Case 1 for every metric except for 90th-percentile position error. This may hint at this method being sensitive to high changes in velocity (a low perilune distance means a high perilune velocity), however it is more likely that Case 1's results are higher simply because it had one more revolution's worth of "blackout" during our testing period than Case 2 did. This assertion is supported by Case 2 performing so much better than Case 3 did, despite Case 3 not having a blackout period and having a lower perilune velocity than Case 2. Case 2's results can be seen in Fig. 4.7 and Case 3's result can be seen in Fig. 4.8.

It should be stated that the highest 90th-percentile position error, that being from Case 3 with the greatest apolune distance, was still lower than the lowest 10th-percentile position error of any case from either of the other methods. This means that for every case tested that the optical navigation performed the best by a wide margin. Its error variation across all test cases was also very small. This, when combined with its stable error behavior, suggests it is a very reliable method for performing autonomous lunar orbit determination when it is an available option. Its reliability also does not seem significantly compromised even when

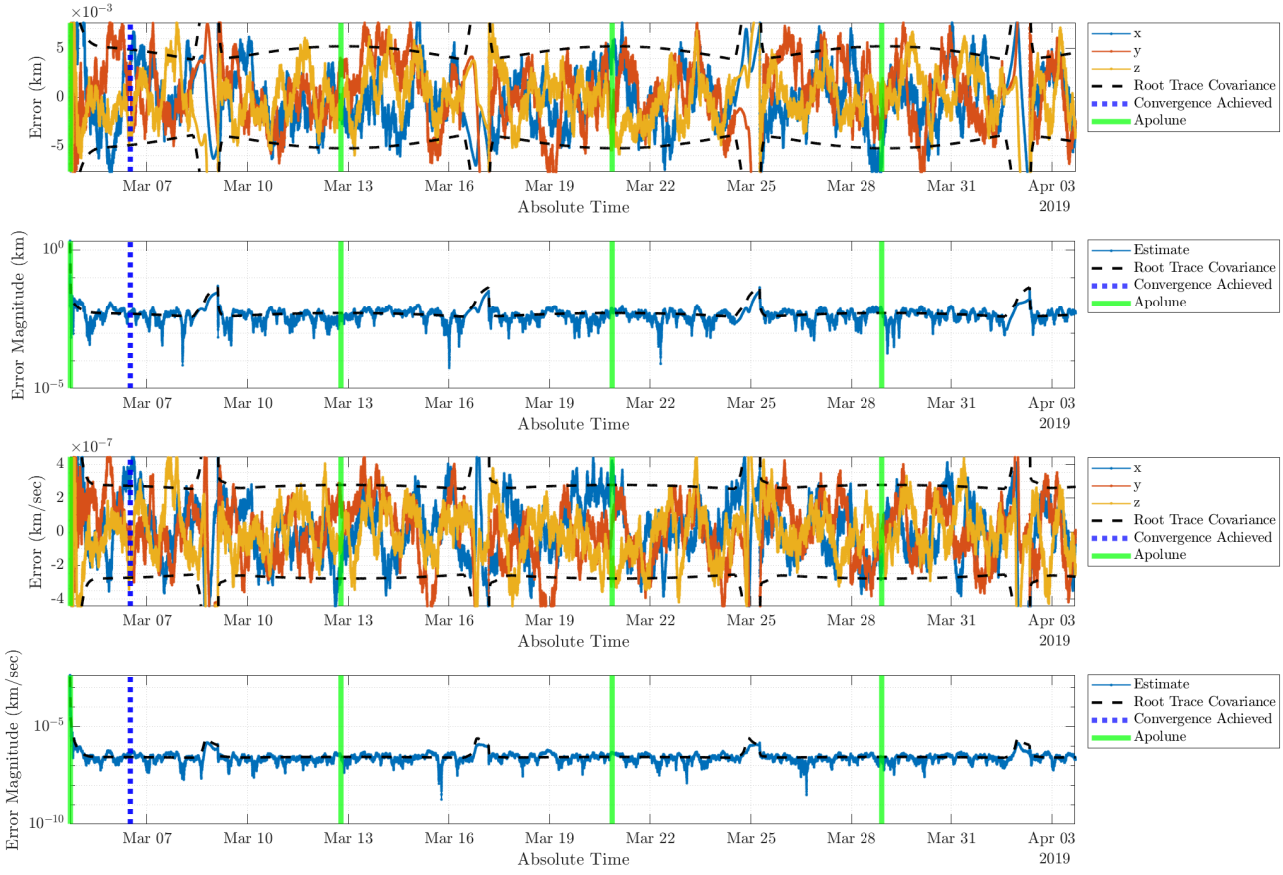

Figure 4.6: Optical Navigation Method Results for Case 1. This case had the most blackout time of any case we tested.

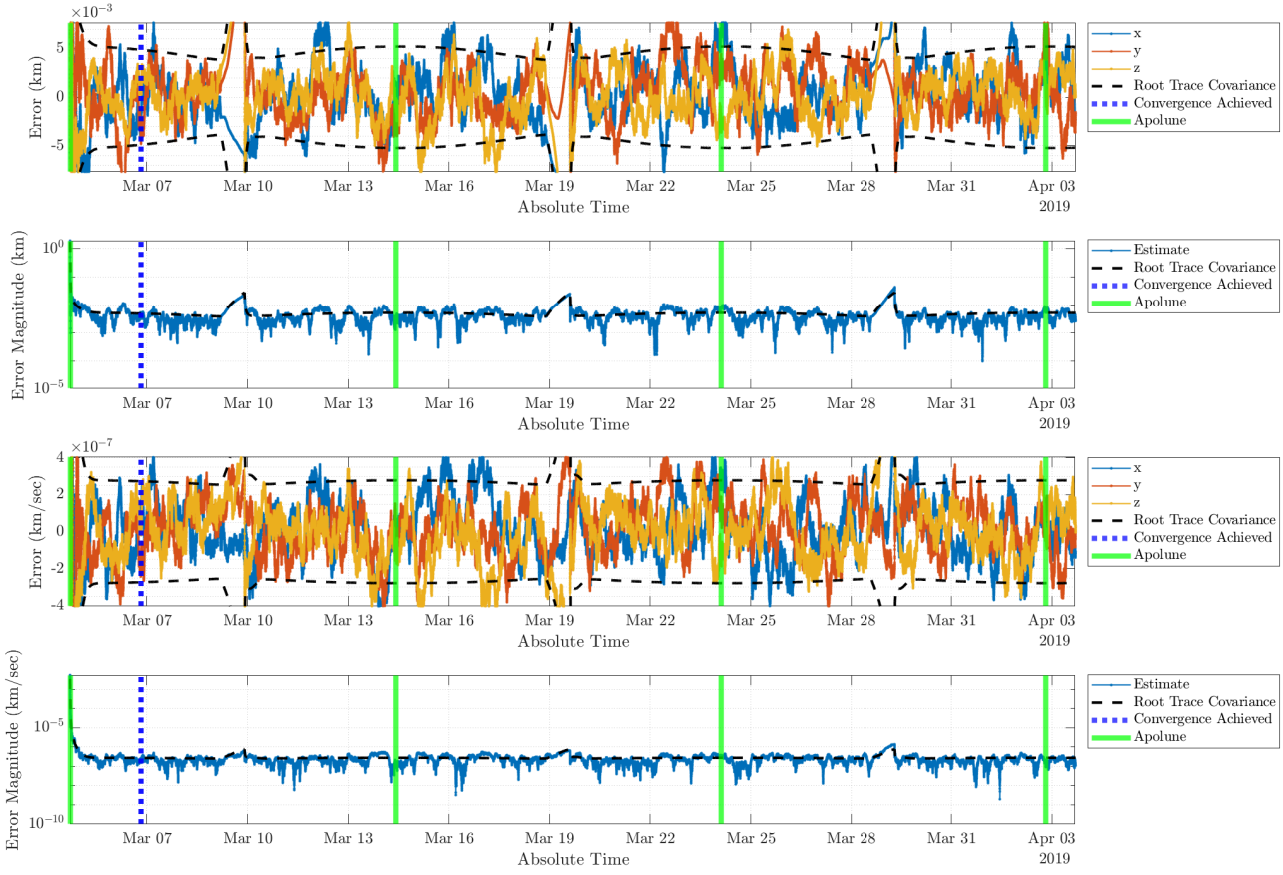

Figure 4.7: Optical Navigation Method Results for Case 2. This case performed the best of all tested cases, despite having blackout time.

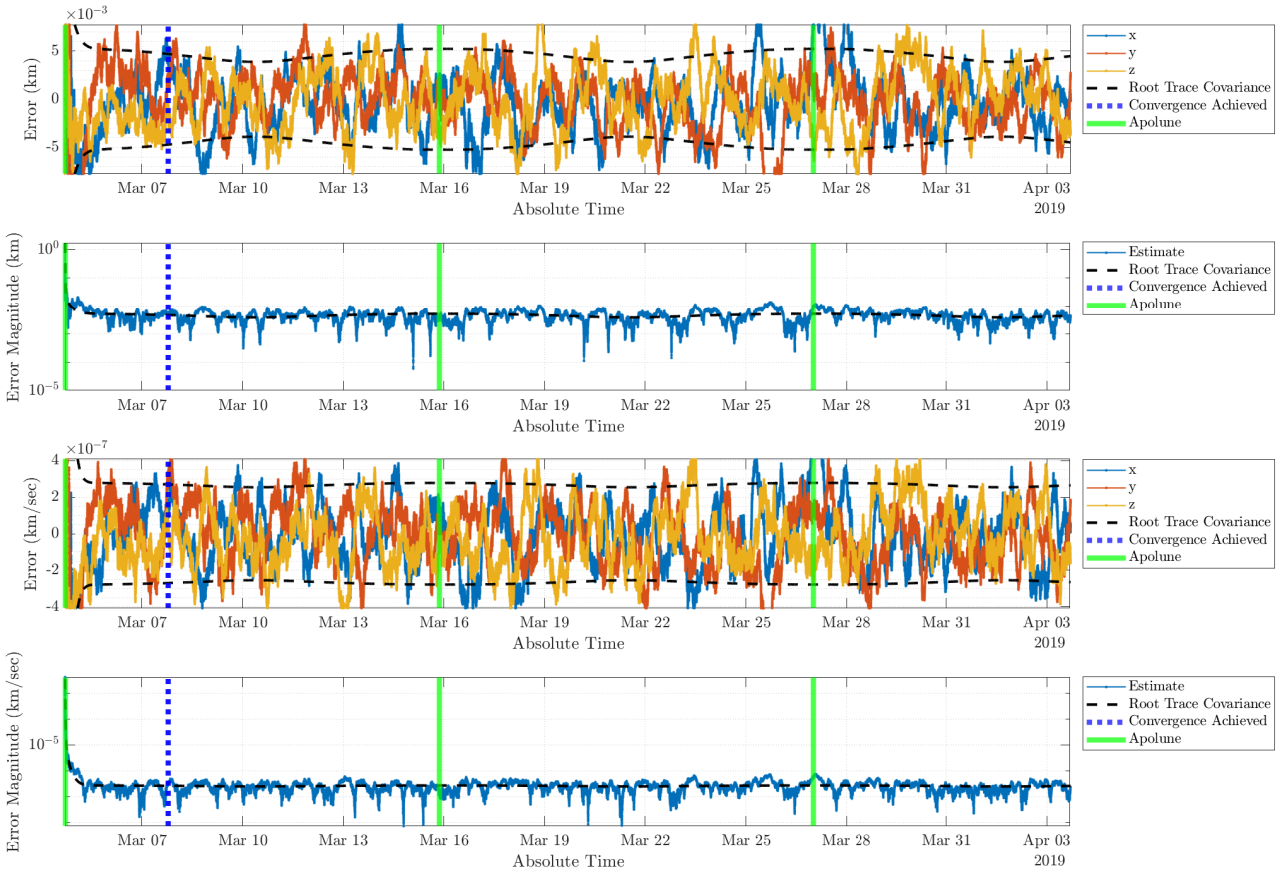

Figure 4.8: Optical Navigation Method Results for Case 3. Case 3 performed worse than Case 2, despite having no blackout period and a lower perilune velocity than Case 2.

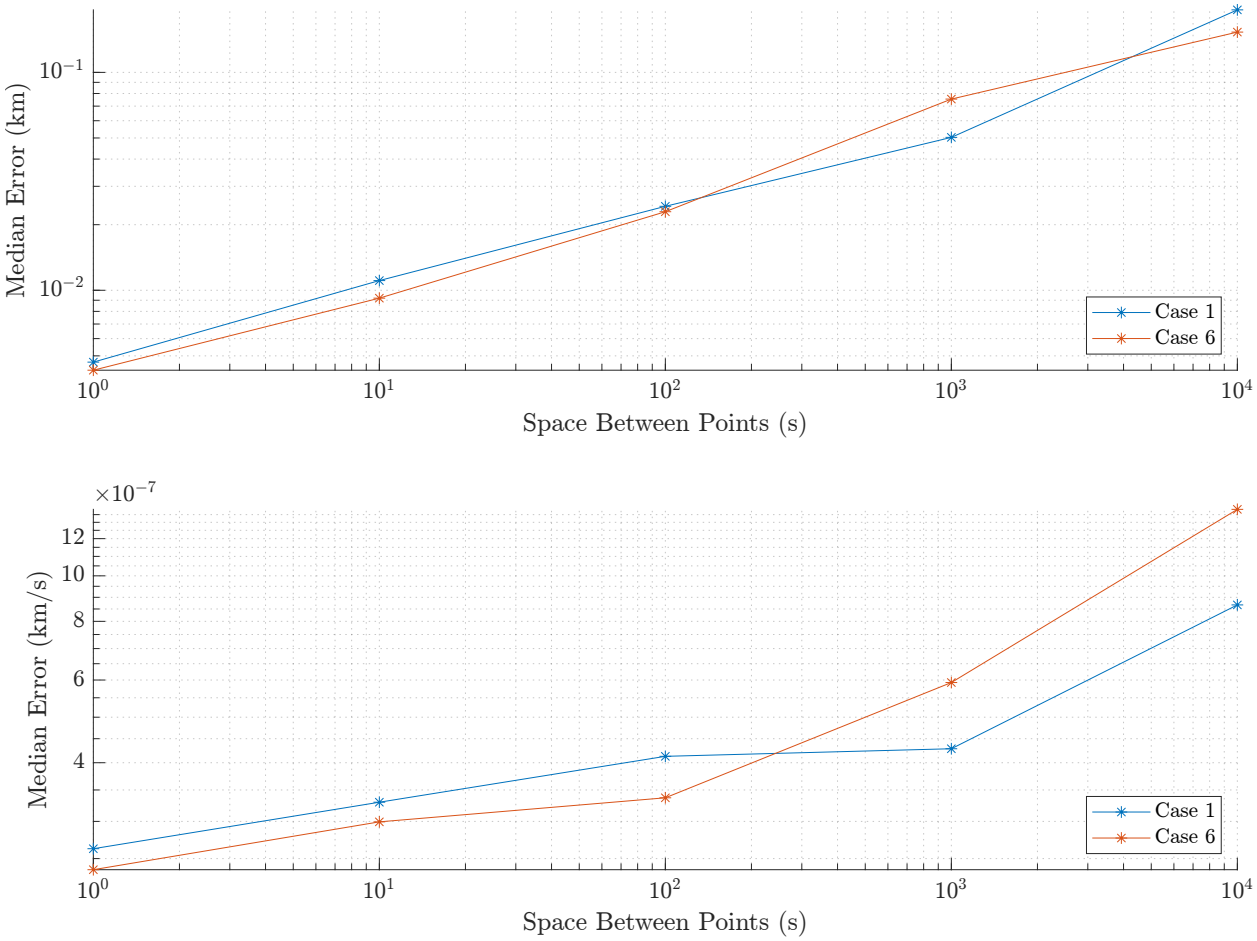

Figure 4.9: Optical Navigation Method Performance with a Varied Time Between Measurements

there is a blackout period on the orbit it is being used for, provided that it is still able to take measurements most of the time. This is supported by real-world evidence, as it was implemented on Artemis missions [21].

This method is the one with the largest assumptions with regard to noise independence. Since so much of the error in optical navigation is dependent on pixelation and other discrete sources of error, which cannot necessarily be averaged out over multiple samples, we suspect that the implemented one-second time step may be too short for the noise to be truly independent, due to how little change in "aim" between captured images would occur with

such a small time step. Therefore, we aim to quantify what independent-noise sample rate is required to achieve a level of performance comparable to the other methods.

To see if the performance of this method was significantly affected if it were to receive measurements less often, 12.4 days′ worth (the period of Case 6) of data was collected with 10 s, 100 s, 1000 s, and 10 000 s in between measurements for Case 1 and Case 6. The results of this testing can be seen in Fig. 4.9. Errors in finding the optical center of the Moon over small time steps may also not be well modeled as random noise, so these results would capture that effect more accurately. Notably, the optical navigation method still has a lower median position error (50th-percentile position error) at Case 1 than either of the other methods with 1000 s between collected points. The same can be said for Case 6, albeit with only 100 s between collected points. It should be noted that the star camera we have used in this study has a frame rate of 55 Hz, so it is not unrealistic to expect that a measurement could be collected once per second, but its reliability even with so much space in between measurements is noteworthy.

Due to the lack of applicable data from a real star camera, some elements of this method could not be simulated. As some examples, [15] talks about how one could determine the optical center of the Moon, different ellipse-fitting algorithms that could be used to more accurately represent the shape of the Moon, and accounting for optical smearing that occurs near the edges of the lenses of the camera. While efforts were taken to account for these effects during testing (see section 3.1.2), it is possible that these factors could generate inaccuracies that would not be captured by our testing.

To see the graphs of the cases that were not discussed here, please see Appendix A.2.

Lunar Mirror Method Results							
		Case 1	Case 2	Case 3	Case 4	Case 5	Case 6
Error (Centile)	Pos. 10% (km)	4.56×10^{-2}	3.80×10^{-2}	6.30×10^{-2}	3.76×10^{-2}	2.53×10^{-2}	4.99×10^{-2}
	Pos. 50% (km)	1.46×10^{-1}	1.35×10^{-1}	1.37×10^{-1}	1.55×10^{-1}	8.57×10^{-2}	1.09×10^{-1}
	Pos. 90% (km)	2.69×10^{-1}	2.76×10^{-1}	2.70×10^{-1}	2.59×10^{-1}	1.88×10^{-1}	1.86×10^{-1}
	Vel. 10% (km/s)	3.38×10^{-7}	3.74×10^{-7}	5.32×10^{-7}	5.72×10^{-7}	3.96×10^{-7}	3.13×10^{-7}
	Vel. 50% (km/s)	7.33×10^{-7}	8.27×10^{-7}	1.05×10^{-6}	9.45×10^{-7}	6.96×10^{-7}	7.73×10^{-7}
	Vel. 90% (km/s)	1.74×10^{-6}	1.53×10^{-6}	1.79×10^{-6}	1.31×10^{-6}	1.12×10^{-6}	1.17×10^{-6}
Time with zero visible mirrors (mins)		1002.27	1648.83	874.55	0.00	0.00	0.00
Time with one visible mirror (mins)		1645.25	1259.07	2106.97	241.20	0.00	0.00
Time with two or more visible mirrors (mins)		40 552.48	40 292.10	40 218.48	42 958.80	43 200.00	43 200.00
Perilune (km)		5.58×10^3	1.79×10^4	2.79×10^4	3.95×10^4	4.56×10^4	4.74×10^4
Apolune (km)		8.67×10^4	8.68×10^4	8.75×10^4	8.15×10^4	7.39×10^4	7.11×10^4
# of Revolutions		3.72	3.09	2.69	2.44	2.42	2.43

Table 4.4: Summary of results for the lunar mirror method

4.2.3 Lunar Mirror Method

As can be seen in Table 4.4, the lunar mirror method performed best on the cases that were the furthest away from the Moon on average (e.g. Case 6). We hypothesize that this is because those cases had the most time when two or more mirrors were available to perform corrections with. It should be stated that you cannot be too far away or your laser ranging system will be unable to reliably perform (this is unsurprising as laser power return scales with $\frac{1}{r^4}$, or $\frac{1}{r^2}$ for each trip), and performing ranging to the different mirrors on the Moon will still not be enough to guarantee observability of the system. It also should be stated that the lunar mirror method performed worse than the optical navigation method for every test case, and was only better than the star occultation method for Cases 5 and 6. Note that the layout of all figures in this subsection are similar to the layout of Fig. 4.3.

Fig. 4.10 shows the results of our filter with the lunar mirror method on Case 6, our case that had the farthest perilune distance. Because of how far it was from the Moon, it was able to see two or more mirrors for the entire testing period, and had the lowest 90th-percentile

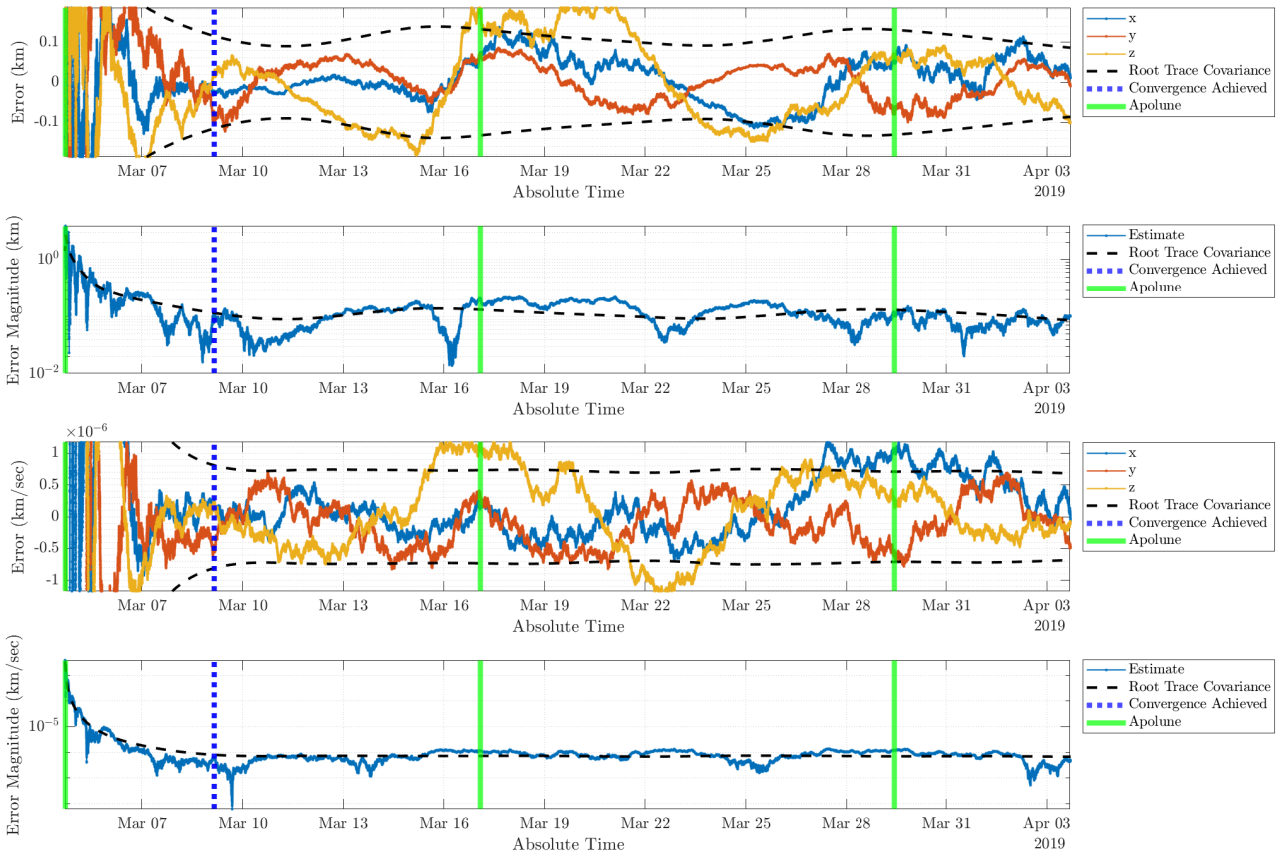

Figure 4.10: Lunar Mirror Method Results for Case 6. This case was the best for this method because it had the highest perilune distance and lowest apolune distance.

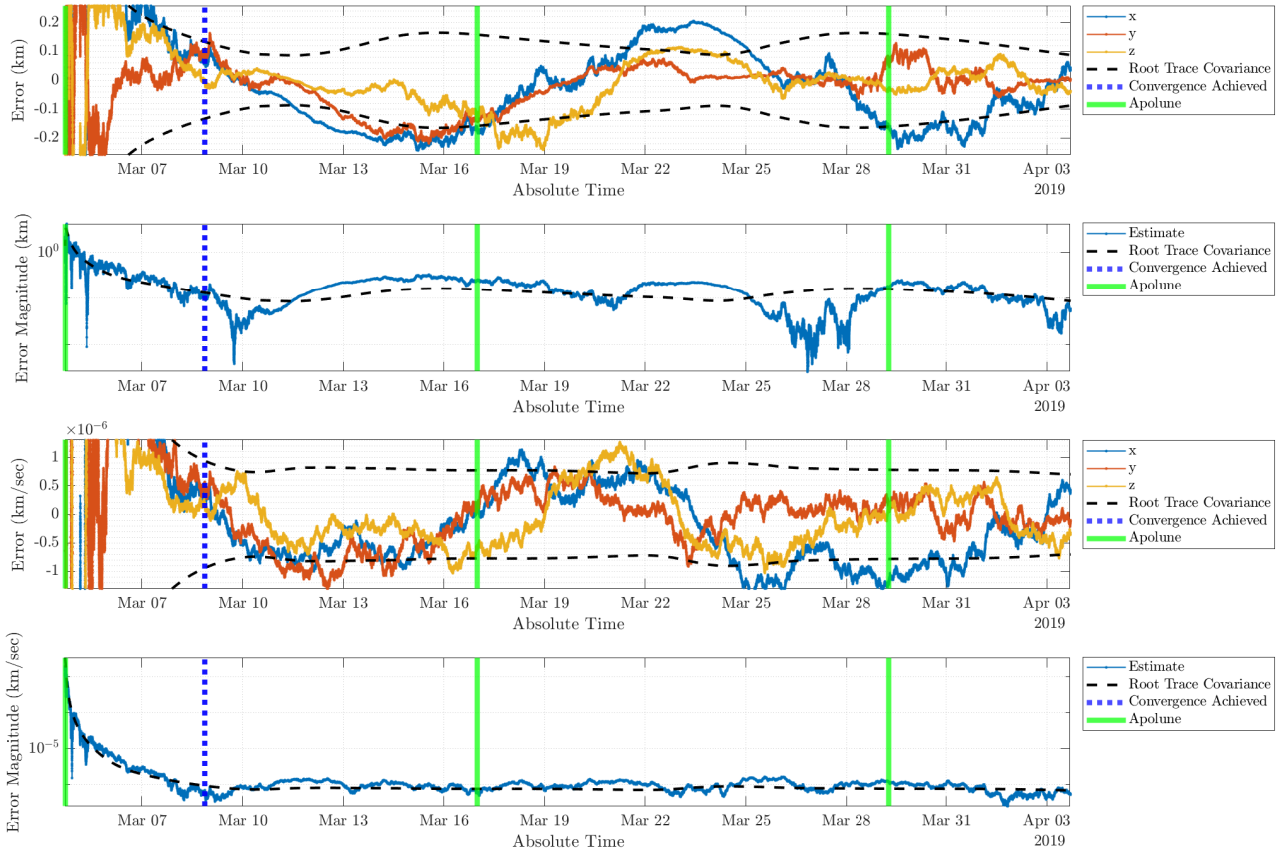

Figure 4.11: Lunar Mirror Method Results for Case 4. This case did not perform well, despite two or more mirrors being visible for nearly the entire testing duration. This suggests this method is sensitive to orbits with a high apolune distance.

position error of all the cases we tested. Case 5 also had access to two or more mirrors for the entire testing period, and performed very similarly to Case 6 as a result.

Fig. 4.11 shows results for the lunar mirror method for Case 4. Despite having nearly the entire testing duration with two or more mirrors visible, its performance was comparable to the cases with less mirror data. This suggests that this method is sensitive to a large apolune distance.

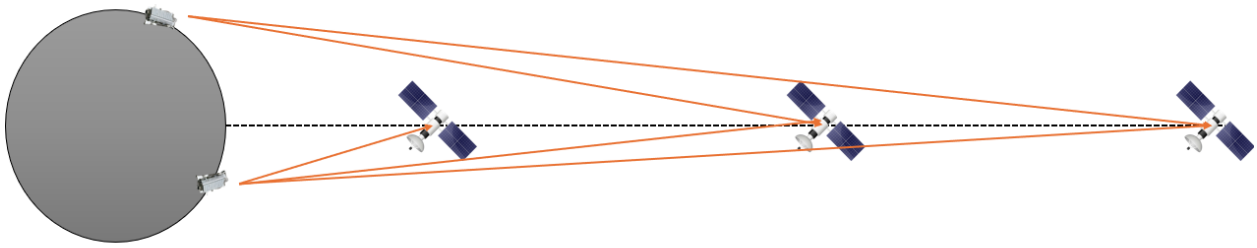

Figure 4.12: Depiction of dilution of precision. By not being far enough away from the Moon, you cannot see enough mirrors, but each mirror becomes less distinguishable from one another if you are too far away from the Moon.

The lunar mirror method performing worse on methods with a large apolune distance is not unexpected. As can be seen in Fig. 4.12, while a satellite that is further away can see more mirrors, the vectors to those mirrors gradually become less distinguishable from each other, and therefore less useful in observing the system. This is a concept called geometric dilution of precision, and it is frequently used in GNSS analysis (as touched on in section 2.1). For the lunar mirror method to function optimally, the satellite using the method needs to be able to see as many mirrors as possible for the entire testing duration, but it also cannot be so far away that there is a high geometric dilution of precision. We hypothesize that this is the cause of the best results in Case 6, since this case had the highest perilune distance as well as the lowest apolune distance.

The uncertainty model used for the lunar mirror method was very conservative. This was deliberate because the sensor system to collect measurements for this method would need to be custom-made, unlike the other methods discussed in this paper, and thus very conservative assumptions needed to be made in the absence of specifications about the sensor system. Although, the lunar mirror method's performance was not as good as both of our other methods for most test orbits. Therefore, we wanted to see how its performance would compare if a more generous uncertainty model was used. To achieve this, we divided our measurement error covariance values for Cases 4 and 6 by 10, 100, 1000, and 10 000 respectively, then evaluated their performance. The results for each of these tests were then compared to the performance yielded by the unaltered measurement error covariance values for these cases (i.e., when the values were divided by 1). These results are shown in Fig. 4.13. The average measurement error standard deviation corresponding to each of these tests is shown in Table 4.5. By dividing the measurement error covariance values by 10 for Case 4, the median position and velocity error improved such that the lunar mirror method surpassed the star occultation method's performance for this case. However, the lunar mirror method

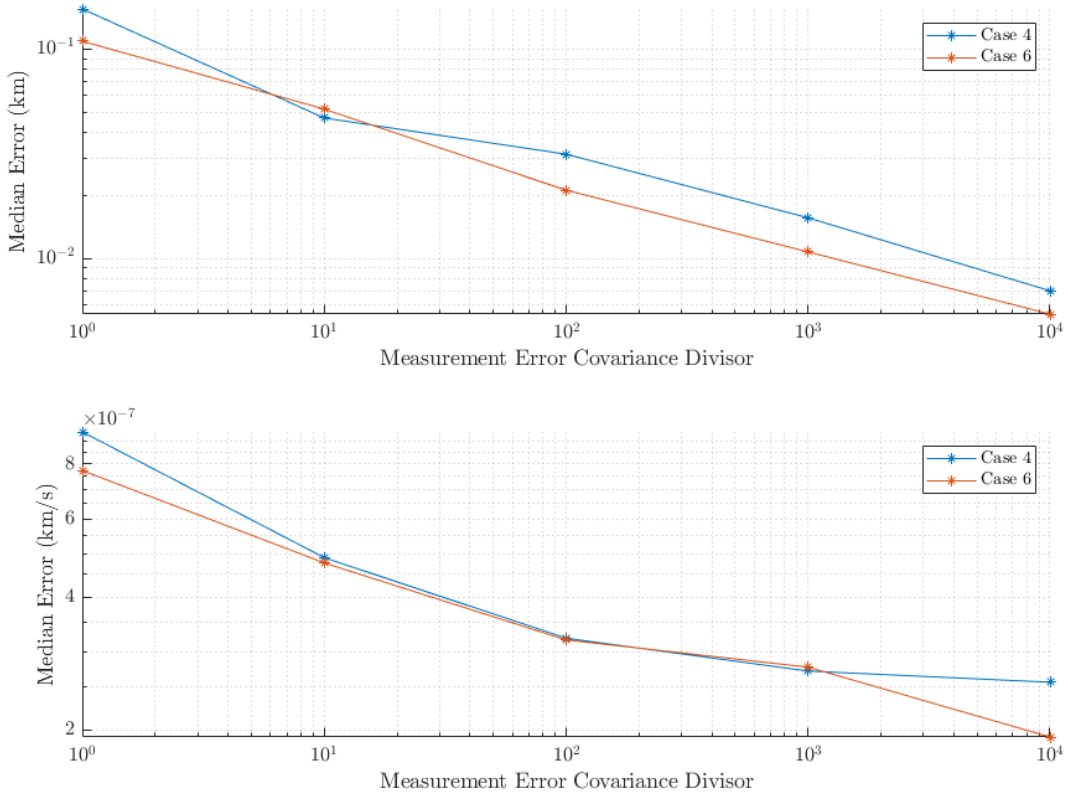

Figure 4.13: Lunar Mirror Method Performance with Smaller Measurement Error Covariance Values

Case Number	Measurement Error Covariance Divisor	Measurement Error Standard Deviation
Case 4	1	0.7401 km
Case 4	10	0.2335 km
Case 4	100	0.0738 km
Case 4	1000	0.0234 km
Case 4	10 000	0.0074 km
Case 6	1	0.7070 km
Case 6	10	0.2230 km
Case 6	100	0.0705 km
Case 6	1000	0.0223 km
Case 6	10 000	0.0071 km

Table 4.5: Table of Average Measurement Error Standard Deviation with Smaller Measurement Error Covariance Values

was still unable to outperform the optical navigation method on either case, even with the measurement error covariance divided by 10 000.

To see the graphs of the cases that were not discussed here, please see Appendix A.3.

Chapter 5

Conclusion

As humanity looks toward the stars once again and seeks to establish a more permanent presence around the Moon, a reliable autonomous lunar orbit determination method will be necessary.

In this study, we tested three methods of autonomous lunar navigation: (1) the star occultation method, (2) optical navigation method, and the (3) lunar mirror method on six different halo orbits in the region around the L_1 Lagrange point of the Earth-Moon system.

It was found that the optical navigation method was the most reliable and best performing method out of the three tested, having the lowest errors in both position and velocity on every test case. It also shows itself to be an affordable option, as it only requires a standard (though high-capability) star camera, as opposed to the laser ranging system required by the lunar mirror method.

Given that both the star occultation method and the optical navigation method require a star camera as their only sensor, it does not seem feasible that one would be able to use the optical navigation method, but unable to use the star occultation method. However, in the case that the lunar mirror method is the only available option, it is recommended to perform ranging to as many mirrors as possible simultaneously or in quick succession, as this maximizes the accuracy of this method. For more data on how this method performs when only one mirror is available, refer to [38].

	Case 1	Case 2	Case 3	Case 4	Case 5	Case 6
Star Occultation Method	1.30×10^{-1}	7.37×10^{-2}	5.60×10^{-2}	8.02×10^{-2}	7.64×10^{-2}	5.93×10^{-2}
Optical Navigation Method	4.68×10^{-3}	3.98×10^{-3}	4.56×10^{-3}	4.33×10^{-3}	4.05×10^{-3}	4.30×10^{-3}
Lunar Mirror Method	1.46×10^{-1}	1.35×10^{-1}	1.37×10^{-1}	1.55×10^{-1}	8.57×10^{-2}	1.09×10^{-1}

Table 5.1: The median position error (in km) for all methods in all cases

As a recap of our results, see Table 5.1. Once again, we can see that optical navigation method is highly accurate for all of our tested orbits, with low errors for each case. Though, it did perform the worst on Case 1, which passes the closest to the Moon. This is because the satellite gets close enough to the Moon that it is not able to see it in its entirety, and thus cannot perform optical ranging. As covered in section 4.2.1, the star occultation method performs better with a higher number of occultations, but is sensitive to the unstable dynamics and rapid changes in velocity that occur with orbits with close lunar approaches. This means the star occultation performs best when in orbits that pass close enough to allow large number of occultations to be observed, but not so close that the estimator becomes numerically instable. The lunar mirror method performs best when far enough away to see a large quantity of lunar mirrors at once, but does not have an apolune distance that is so far away that the GDOP to these mirrors becomes too high for precise navigation. Cases 5 and 6 had the highest perilune distances of our sample orbits, but also the lowest apolune distances, and the lunar mirror method performed the best on these two cases as a result.

5.1 Limitations

While much was learned from this study, it does leave a few unanswered questions.

Our dynamics model was simplistic, and could be made much more realistic with the addition of a spherical harmonic gravity model, solar and lunar albedo radiation pressure accelerations, or other acceleration perturbations. We used the CR3BP, which assumes the

Moon is in a perfectly circular orbit, and that the Earth and Moon are point masses. We assumed the Moon was a perfect sphere, and incorporating an accurate terrain model would affect the performance of all of our measurement methods.

For the lunar mirror method, we also assumed that the mirrors did not move in the synodic frame, which is inaccurate due to the Moon's optical librations relative to Earth. It was also assumed that ranging could be performed to a mirror if it was within sight of the satellite, when in reality you would have to be within an angular cone over the mirror based on the elevation restrictions and tilted normal vectors specific to each LRRR.

For the optical navigation method, we did not use realistic star camera data (i.e., we used realistic optical properties, but not fully simulated test images), and thus could not accurately simulate all potential sources of non-Gaussian and correlated error within this study. While efforts were taken to account for errors that we could not simulate, we had to assume that these errors would be Gaussian and uncorrelated, and this may not be accurate.

We also did not account for lighting conditions on the surface of the Moon, which would drastically change the uncertainty parameters of collected measurements for each method depending on whether parts of the Moon were illuminated when they were collected. The star occultation method would struggle to record occultations that occur on an illuminated lunar limb, the optical navigation method would struggle to accurately define the elliptical outline of the Moon if significant portions of its visible side were dark, and the lunar mirror method would struggle to gather ranging measurements to mirrors in sunlight. Notably the star occultation method and optical navigation method require the same sensor system to operate, which is a star camera, and have opposite lighting conditions that are considered "favorable" to each of them.

5.2 Future Work

To expand on what has been covered in this study, much additional work could be done.

5.2.1 Further Testing With These Measurement Methods

In the future, it would be interesting to see how accurate a measurement model that combines the star occultation method and optical navigation method would be, as they both require a star camera to function and have distinct lighting requirements. It is theorized that the star occultation method could help achieve an extremely accurate solution in perilune, potentially when operating too close to the Moon to use the optical navigation method, and then the optical navigation method will maintain this accurate solution in apolune when occultations are more sparse.

Because it was determined that the optical navigation method was superior to the other methods in all of our test cases (at least for our noise assumptions), work should be done to test this method's effectiveness with realistic star camera data. Even though efforts were taken to account for noise introduced by using star camera images, such as the noise in finding the true optical center of the Moon, these perturbations were presumed to be Gaussian and uncorrelated when this may be inaccurate.

The lunar mirror method was also only tested with the assumption that ranging could be performed to multiple mirrors at once. Further testing should be done with ranging only being done to a single mirror to see how this method's accuracy is affected. Also, unlike the other two methods that were tested using specifications from a commercially-available star camera, the sensor system for the lunar mirror method would be a bespoke one. For this reason, it would make sense to test it with different uncertainty parameters such that

designers that wish to use this method can understand what performance they can expect from the method given their sensor system's specifications.

All three methods should also be tested when accounting for different lighting conditions on the lunar surface, as each method's performance would be significantly affected. In [13], occultations that occurred on the illuminated side of the Moon were removed entirely as it would be much harder to detect the moment when the star went behind the Moon. It would be good to test the star occultation method with occultations on the illuminated side of the Moon either completely removed, or with much higher uncertainty values than occultations that occur on the dark side of the Moon. For the optical navigation method, it would be much harder to determine the outline of the Moon within the star camera images if it was not entirely illuminated. For the lunar mirror method, it would be much more difficult (or impossible [28]) to detect returning photons from the LRS if the area within the detector's field of view was illuminated. A larger field of view for the detector would make it easier to track mirrors, and potentially make it possible to track multiple mirrors at once, but it would also mean there would be a greater chance that no measurements could be collected due to excessive reflected sunlight within the field of view.

Testing in accurate light conditions will also allow us to gain a better appreciation for how combining measurement methods could help compensate for the weaknesses displayed by one method. For example, it is much more difficult to collect occultations when the Moon is illuminated, but the optical navigation method can collect more accurate measurements during this time. The inverse is also true to an extent, as it is much harder to do optical ranging when the Moon is dark, but much easier to collect occultations. This could lead to interesting behavior in the case where the Moon is illuminated, so occultations could not be collected, but the satellite is also too close for the Moon to fit within the field of view of the star camera, so optical ranging is not possible either.

5.2.2 Simulation Improvements and Worthwhile Test Cases

This study used the CR3BP, which assumes that the Earth and Moon are point masses when calculating the gravitational acceleration of the satellite and ignores all other sources of acceleration. It would be more accurate to use spherical harmonic gravity models for both the Earth and Moon. The tidal acceleration effects of the Sun should also be included, along with solar radiation pressure and lunar albedo radiation pressure. We also should incorporate Moon orientation data and a lunar topographical map for more accurate limb and LRRR positions

Our test cases were also narrow in scope, and testing in other halo orbits, Lyapunov orbits, distant retrograde orbits, and butterfly orbits would help to identify more strengths and weaknesses of our measurement methods. This study also simulated perfect orbits with no control, and it would be enlightening to see how the measurement methods perform with imperfect orbits that utilize realistic station-keeping.

5.3 Final Thoughts

For performing autonomous lunar orbit determination, the optical navigation method outperformed the other methods in our tested cases by a considerable margin. The star occultation method proved itself to be reliably accurate on the cases with a low perilune distance, as this caused the most occultations. It would seem that the optical navigation method and star occultation method could easily be combined to great effect, as they both use the same sensor to take their measurements and their respective strengths counter their respective weaknesses. It was also noteworthy that the lunar mirror method seemed to be more sensitive than the other methods tested to orbits with a high apolune distance.

Appendices

Appendix A

All Results

In this chapter, all of the test results from every measurement method for every test orbit are shown. We first will cover all of the test results for the star occultation method, then the test results from the optical navigation method, then the results from the lunar mirror method.

A.1 Star Occultation Method Results

Here we will show all of the test results from all of the test orbits for the star occultation method. They will be shown in ascending order for Case 1-6.

A.2 Optical Navigation Method Results

Here we will show all of the test results from all of the test orbits for the optical navigation method. They will be shown in ascending order for Case 1-6.

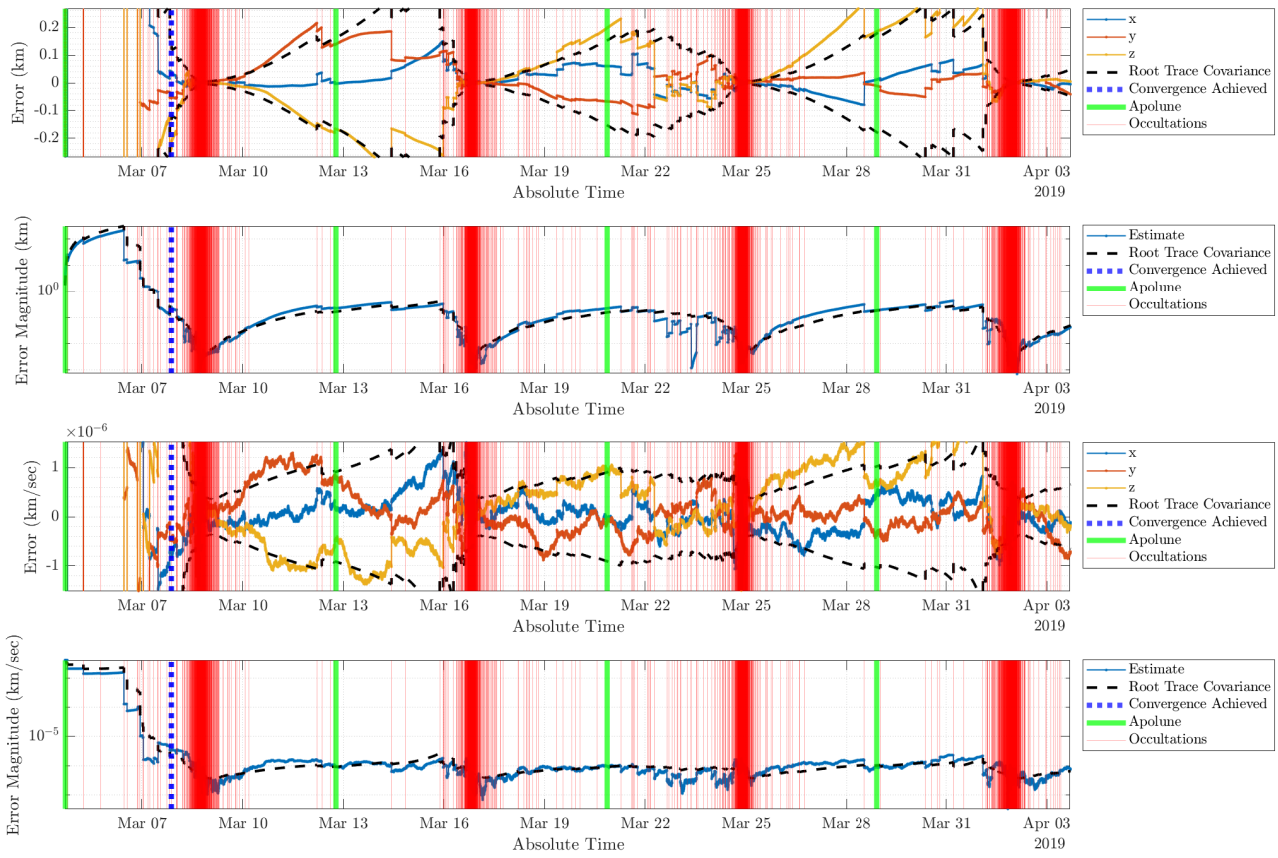

Figure A.1: Star Occultation Method Results for Case 1

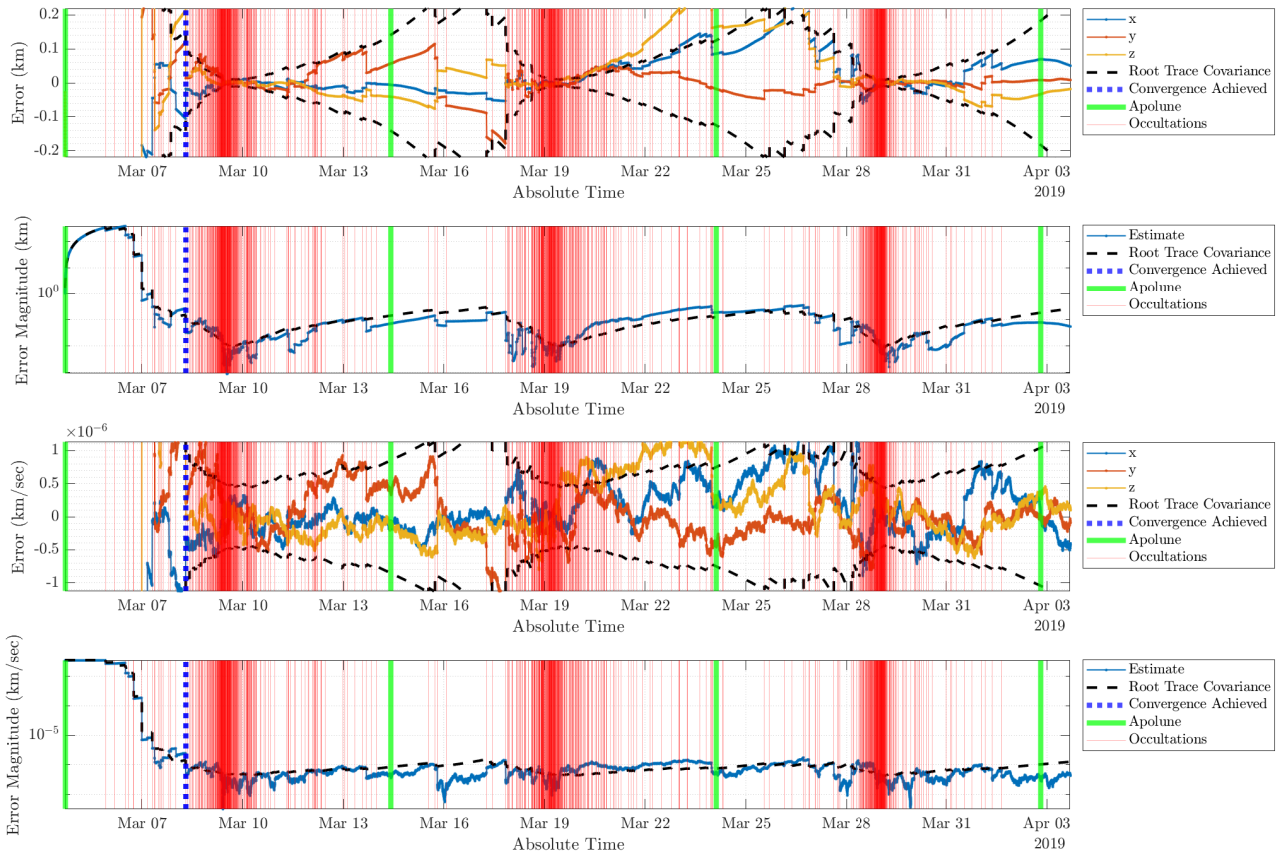

Figure A.2: Star Occultation Method Results for Case 2

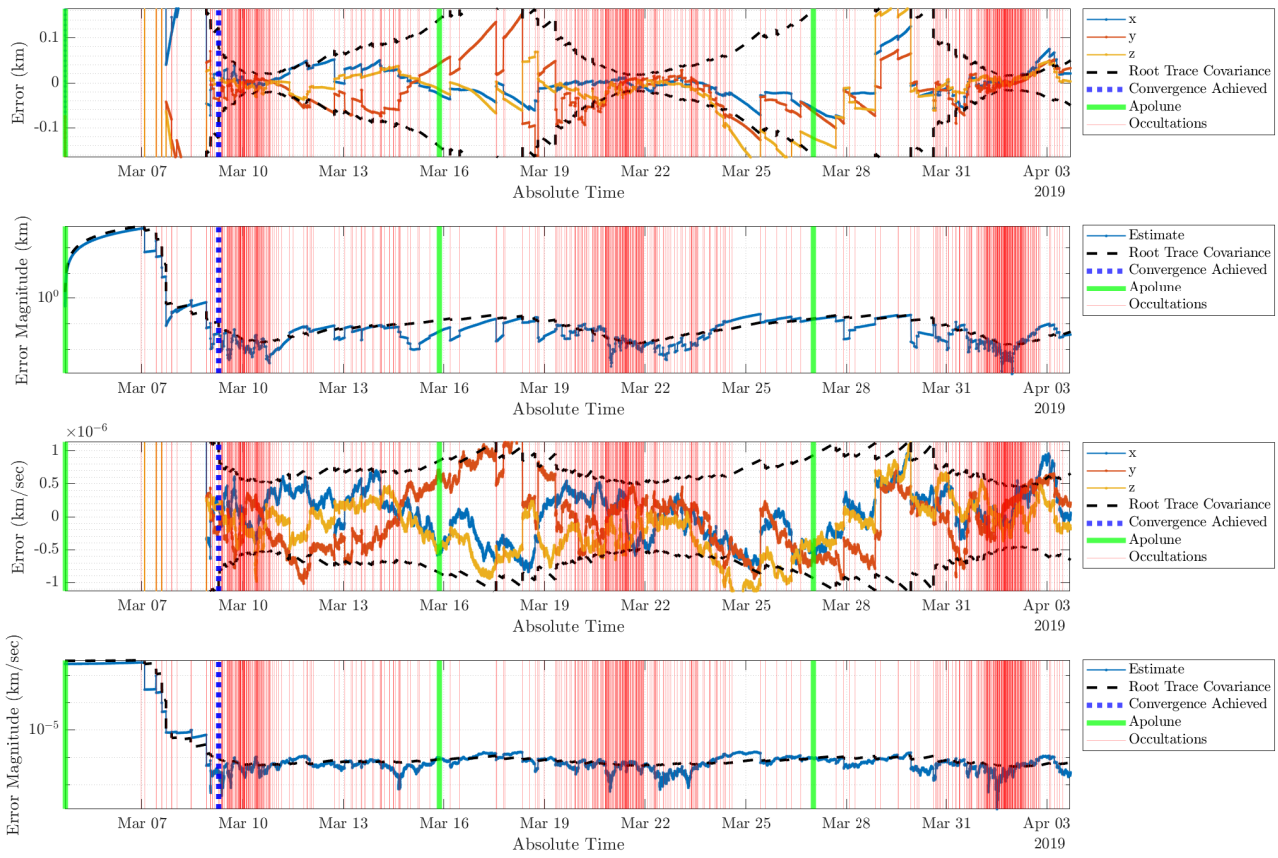

Figure A.3: Star Occultation Method Results for Case 3

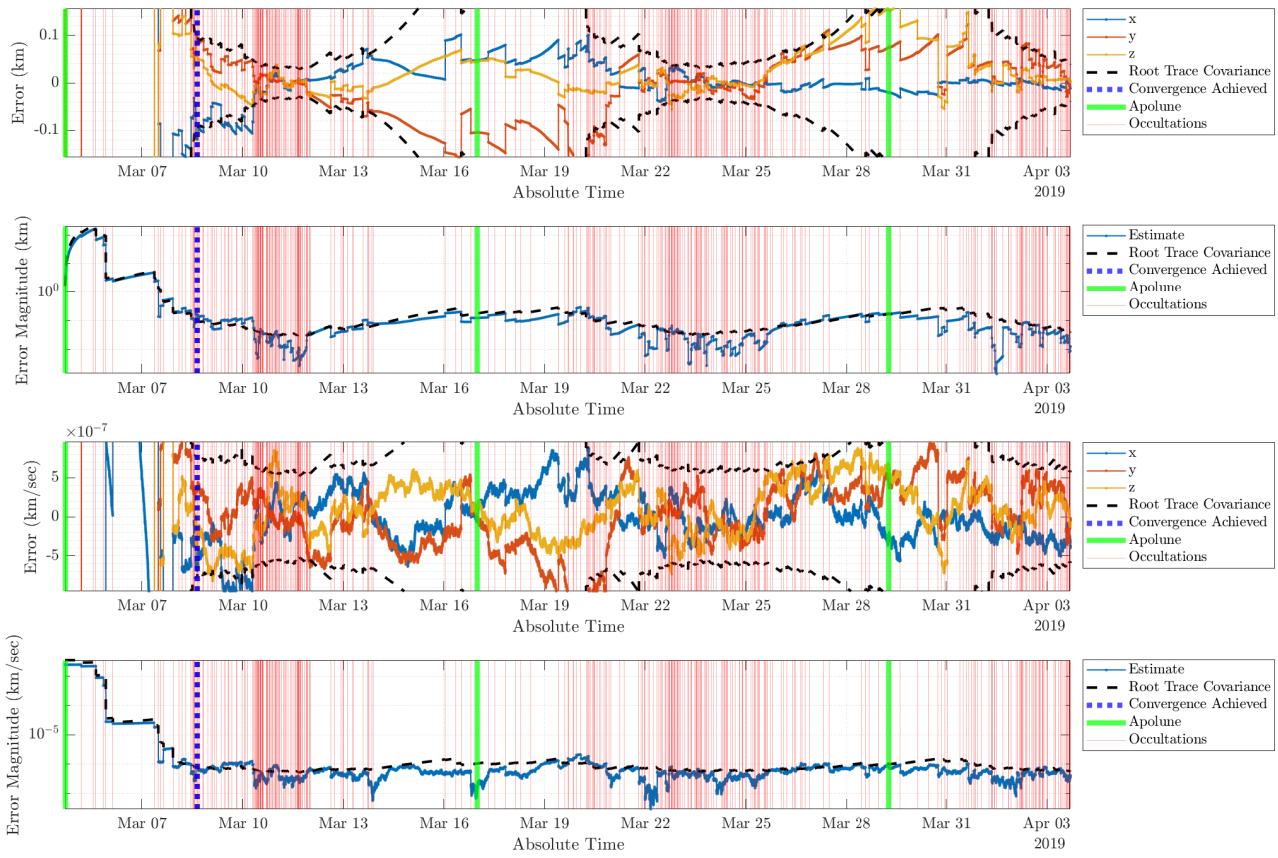

Figure A.4: Star Occultation Method Results for Case 4

Figure A.5: Star Occultation Method Results for Case 5

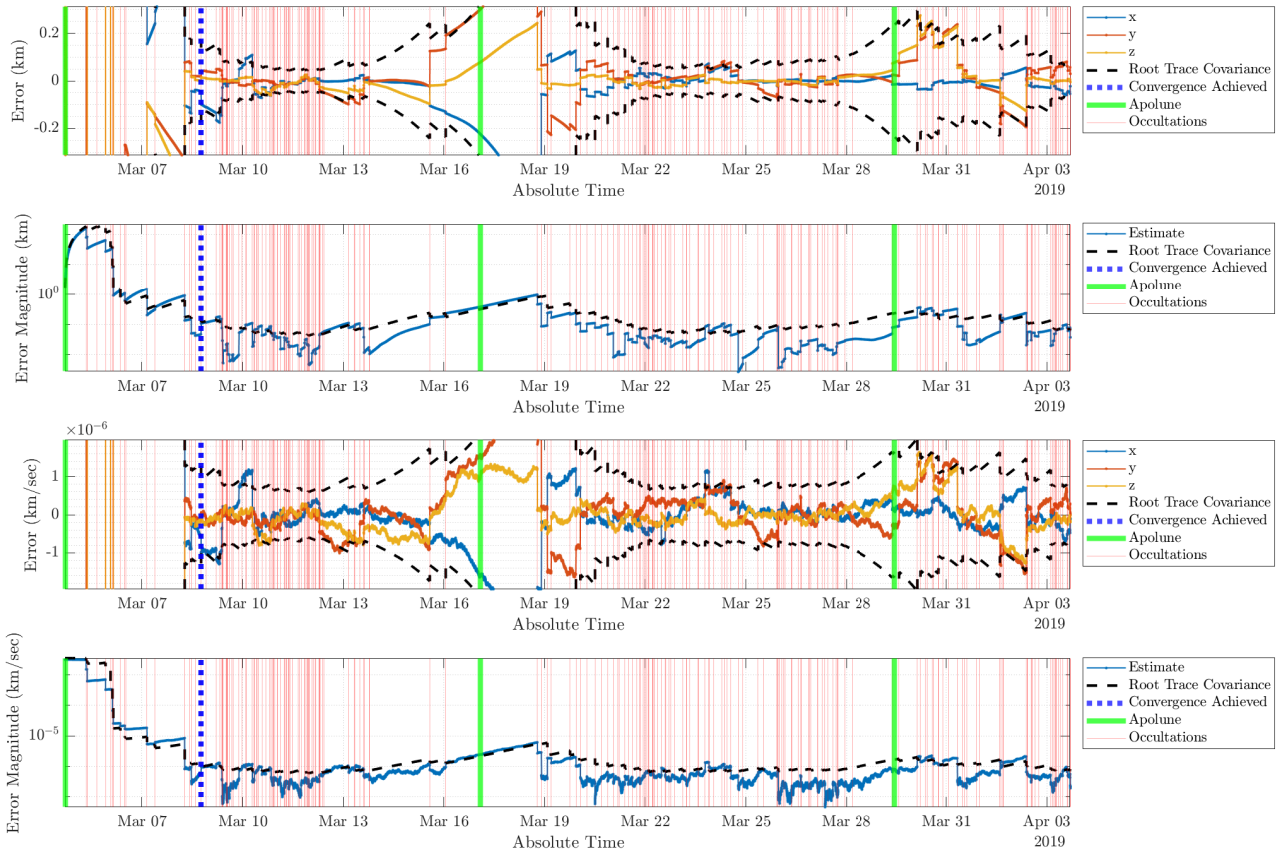

Figure A.6: Star Occultation Method Results for Case 6

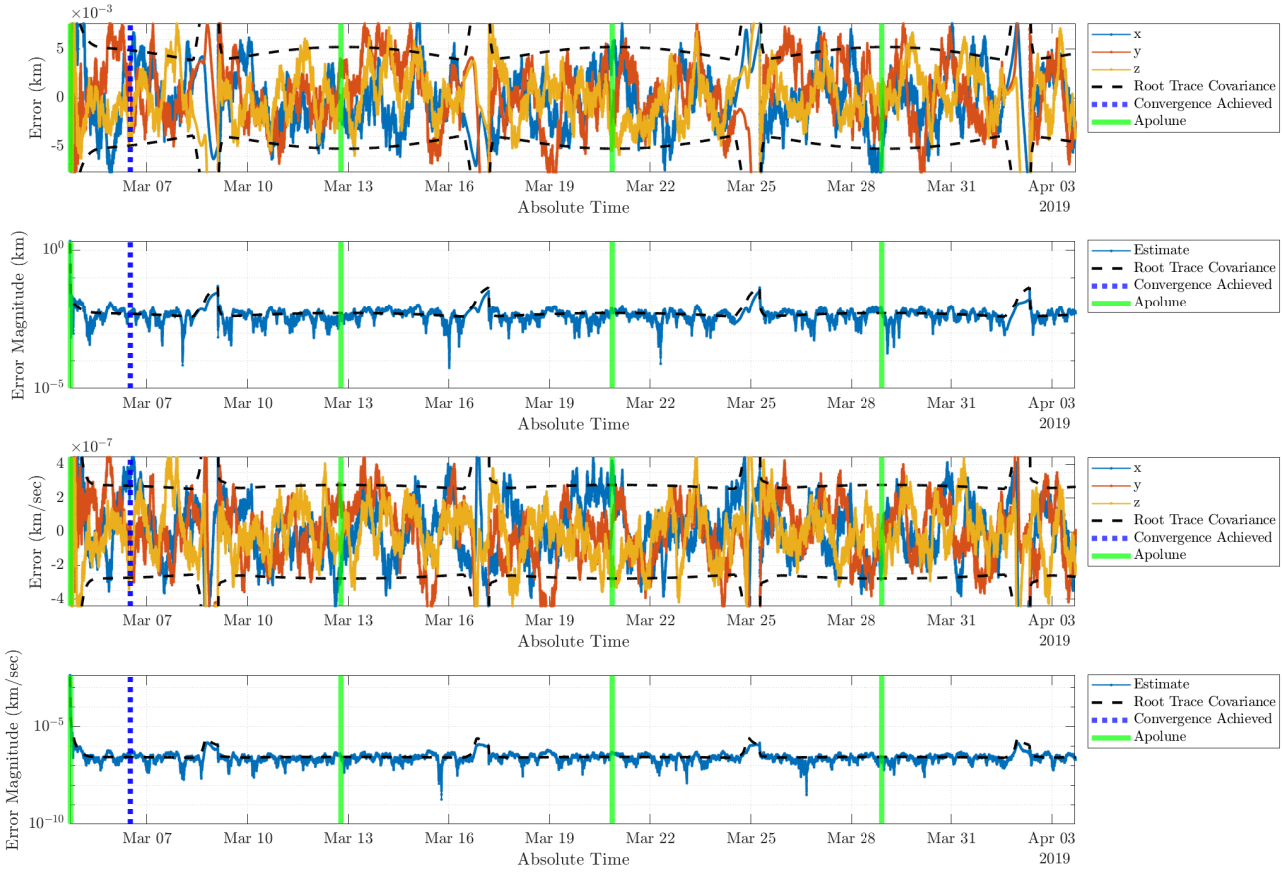

Figure A.7: Optical Navigation Method Results for Case 1

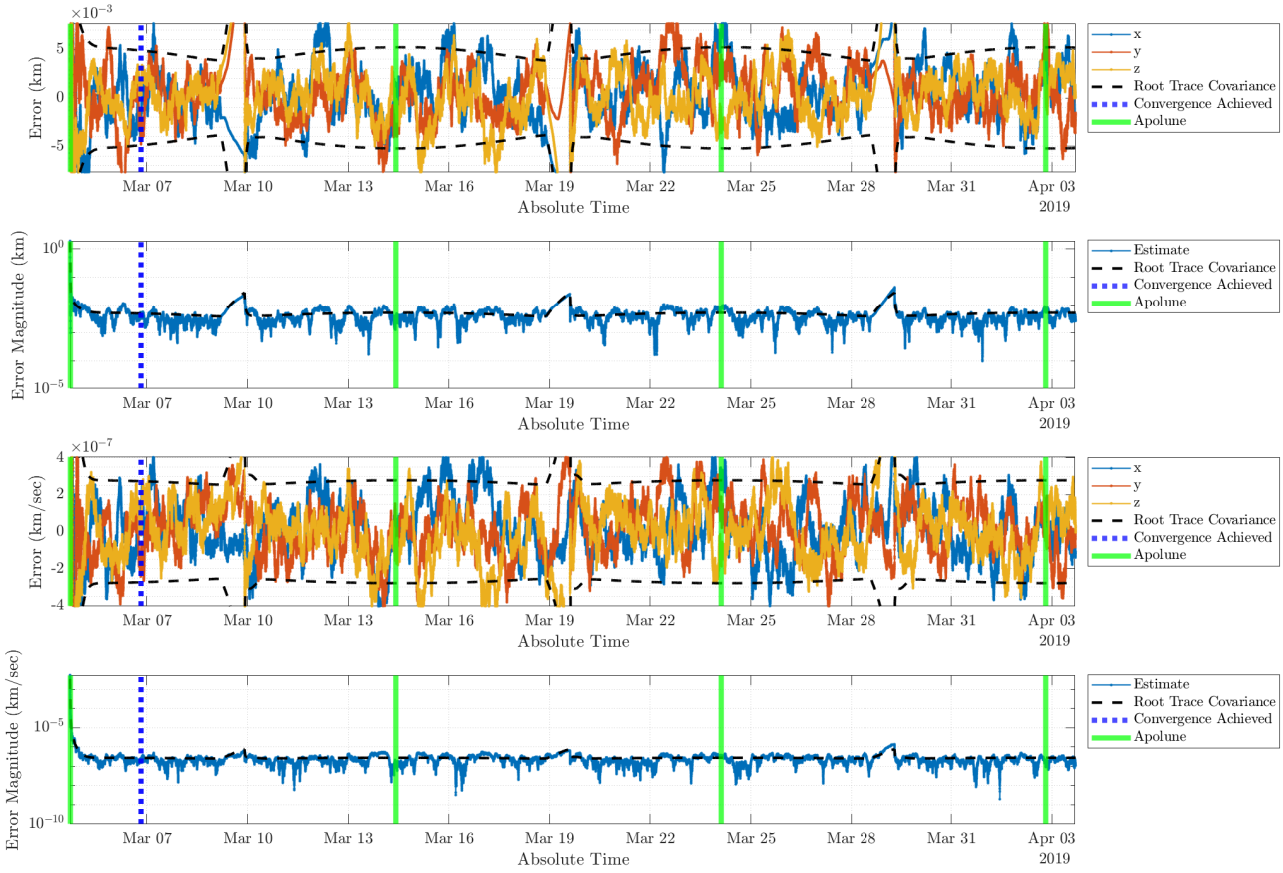

Figure A.8: Optical Navigation Method Results for Case 2

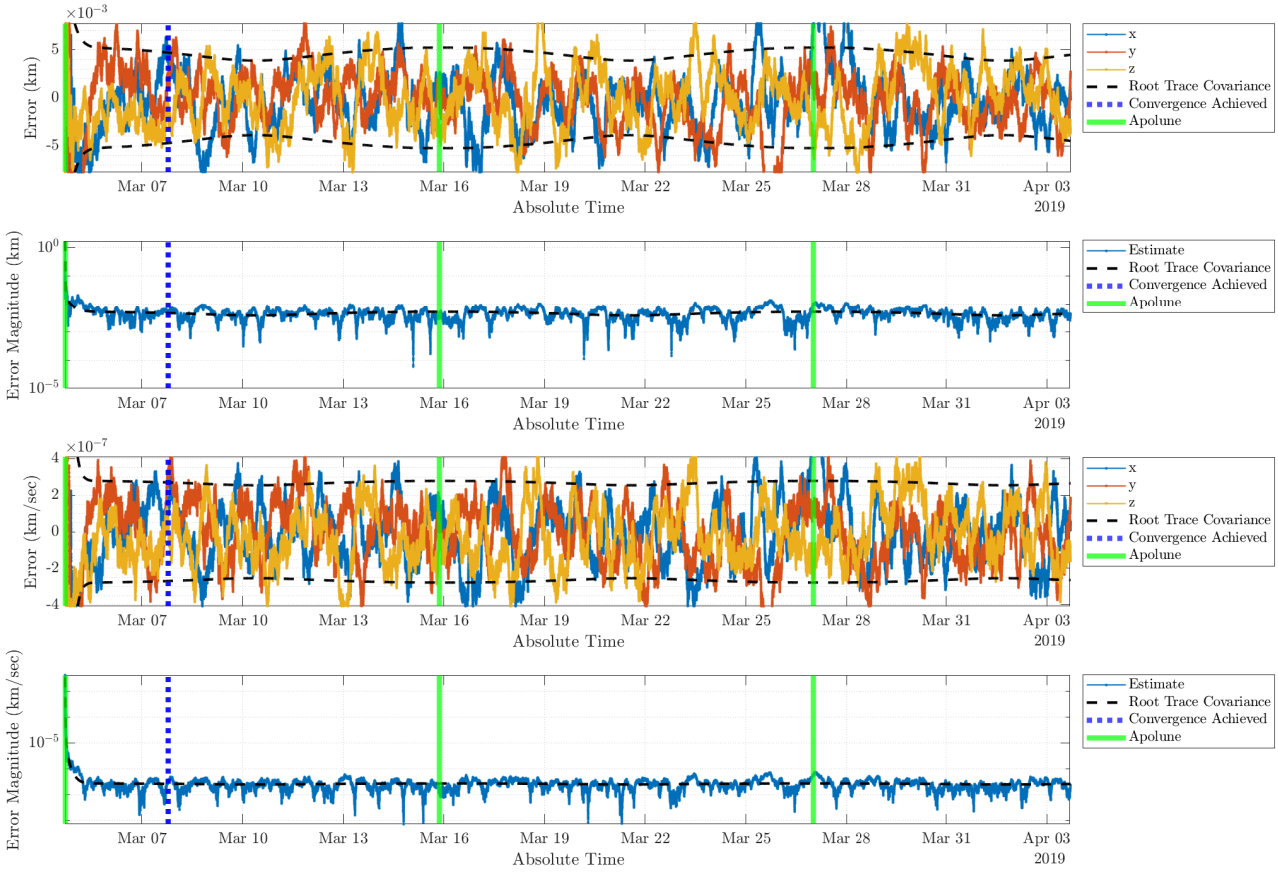

Figure A.9: Optical Navigation Method Results for Case 3

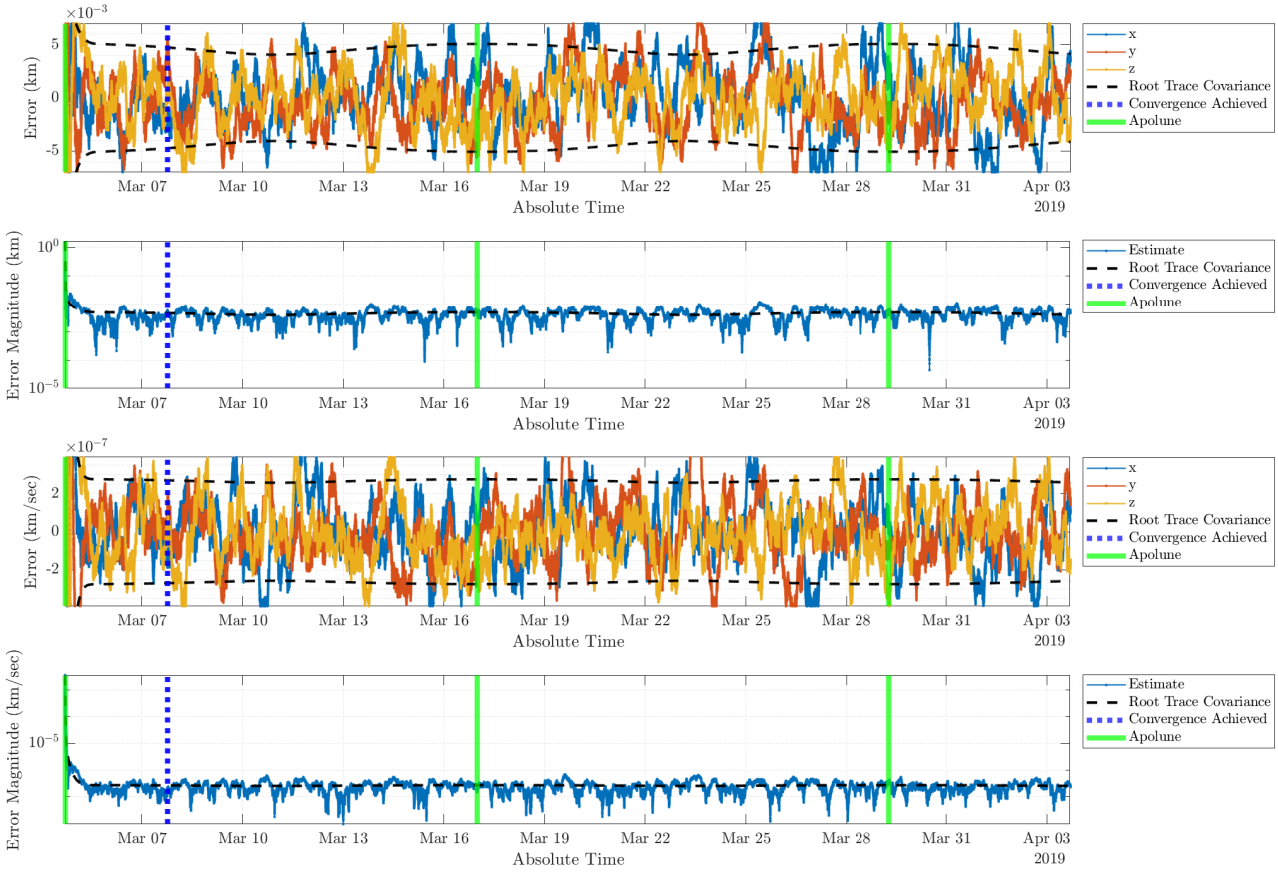

Figure A.10: Optical Navigation Method Results for Case 4

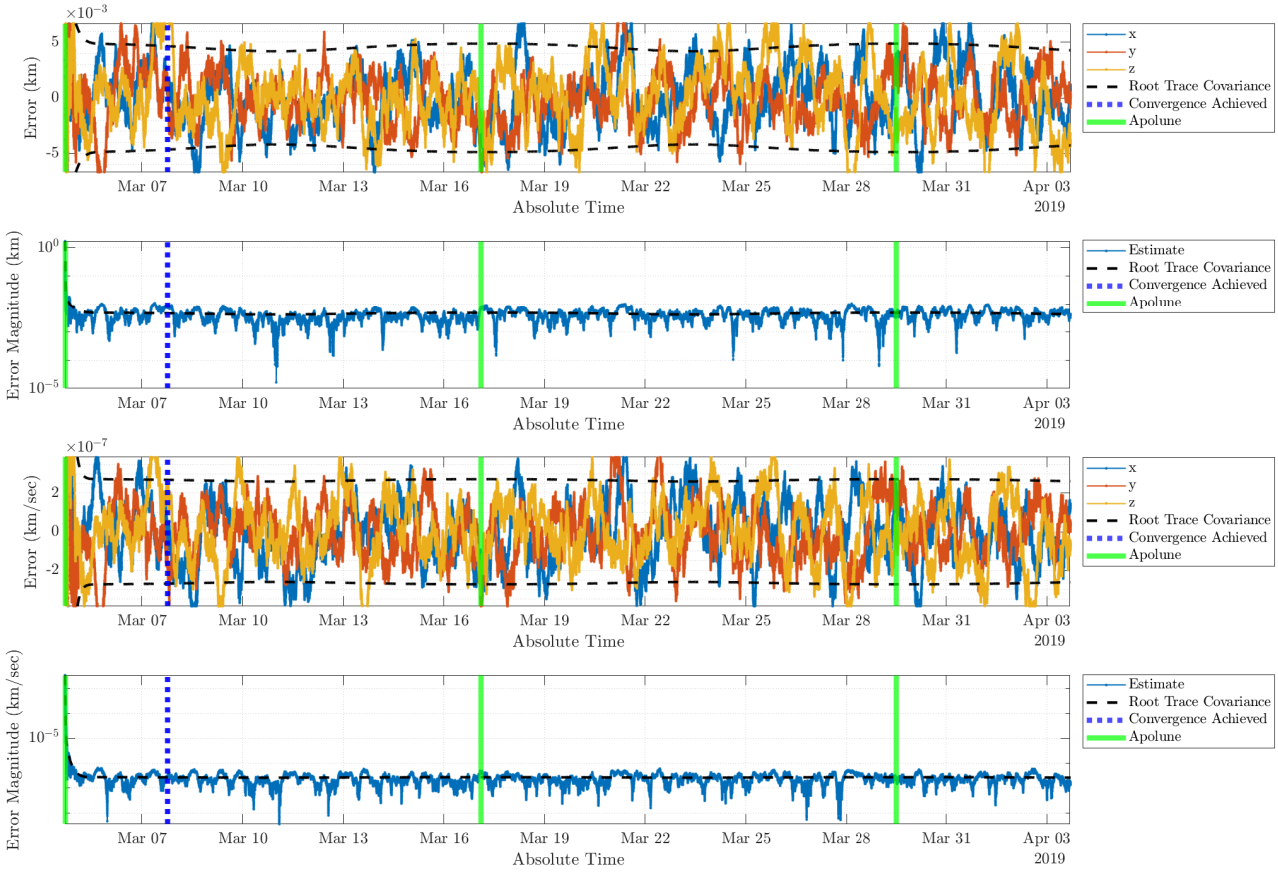

Figure A.11: Optical Navigation Method Results for Case 5

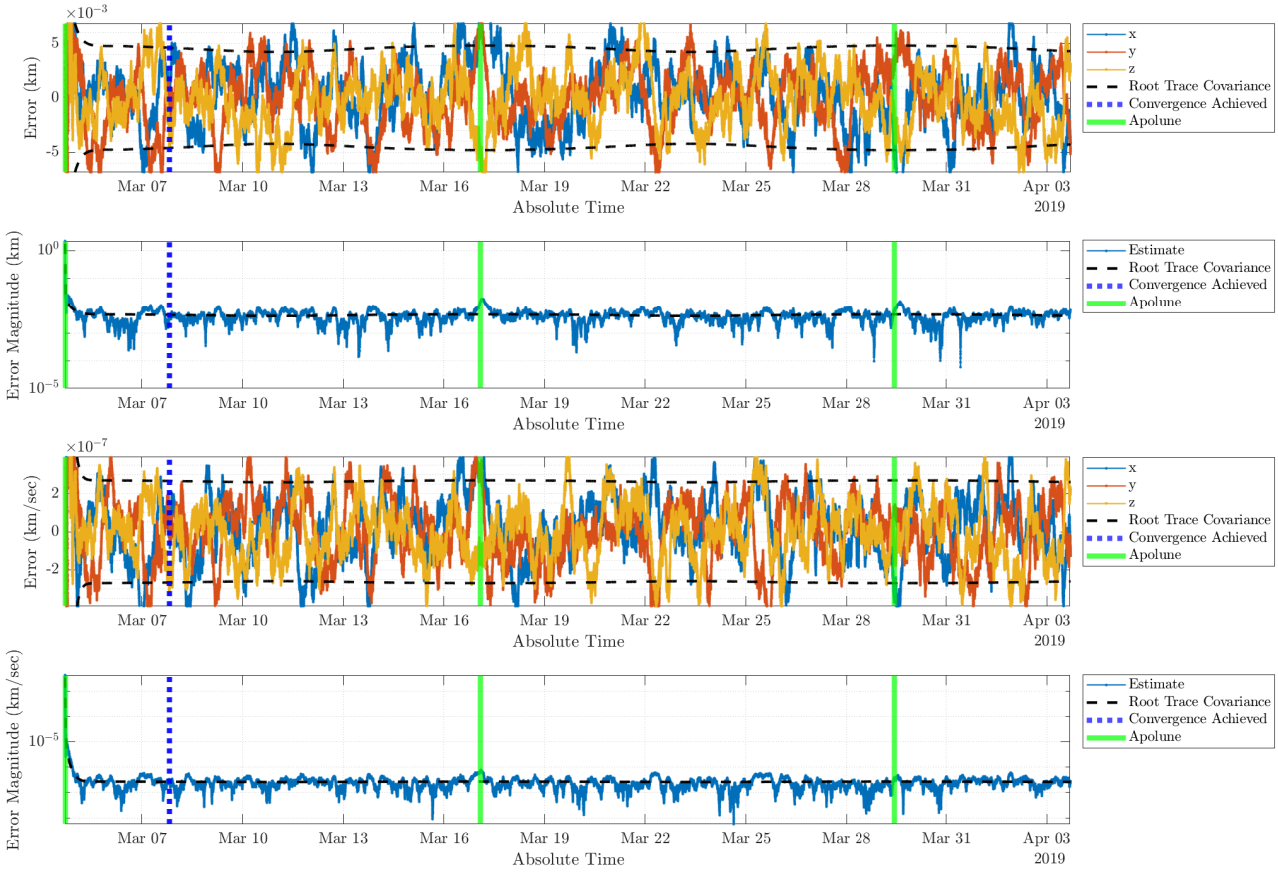

Figure A.12: Optical Navigation Method Results for Case 6

Figure A.13: Lunar Mirror Method Results for Case 1

A.3 Lunar Mirror Method Results

Here we will show all of the test results from all of the test orbits for the lunar mirror method. They will be shown in ascending order for Case 1-6.

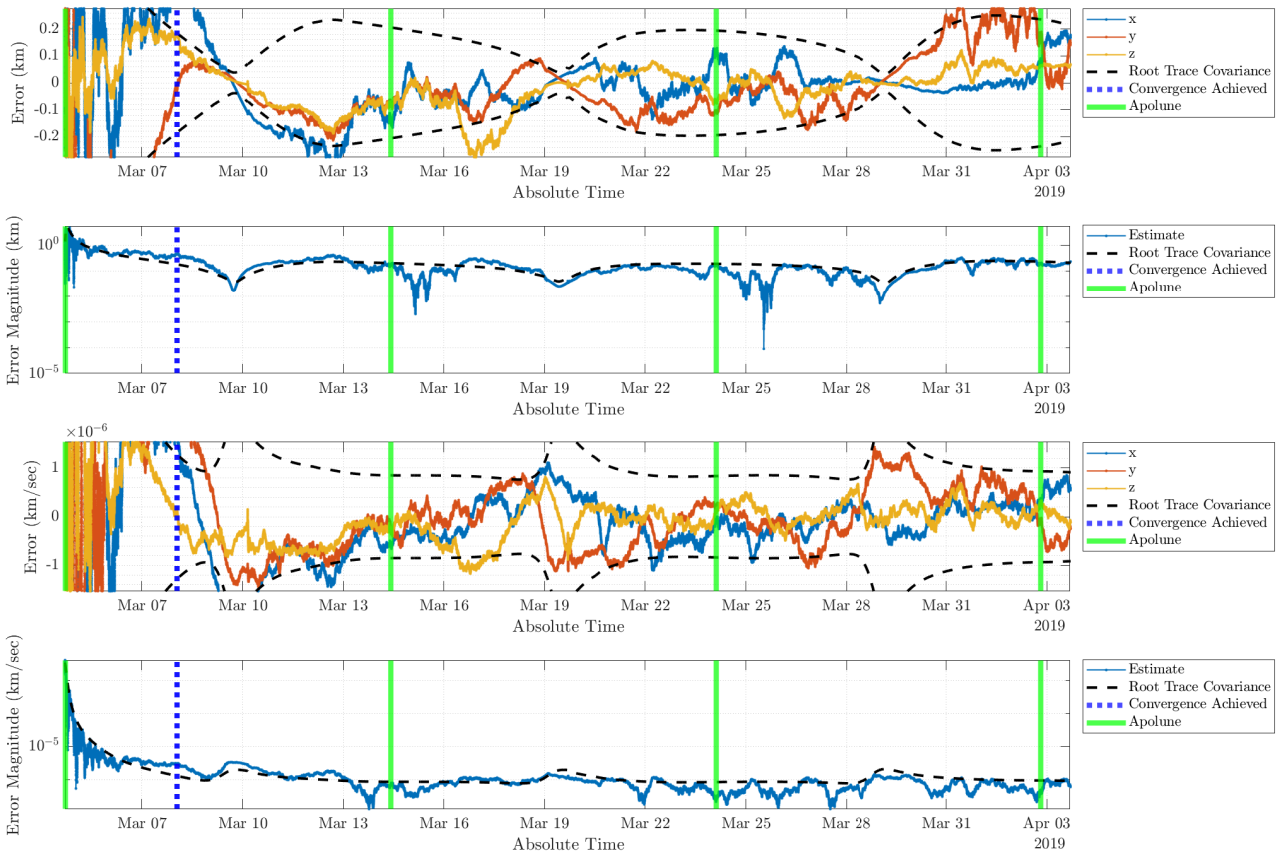

Figure A.14: Lunar Mirror Method Results for Case 2

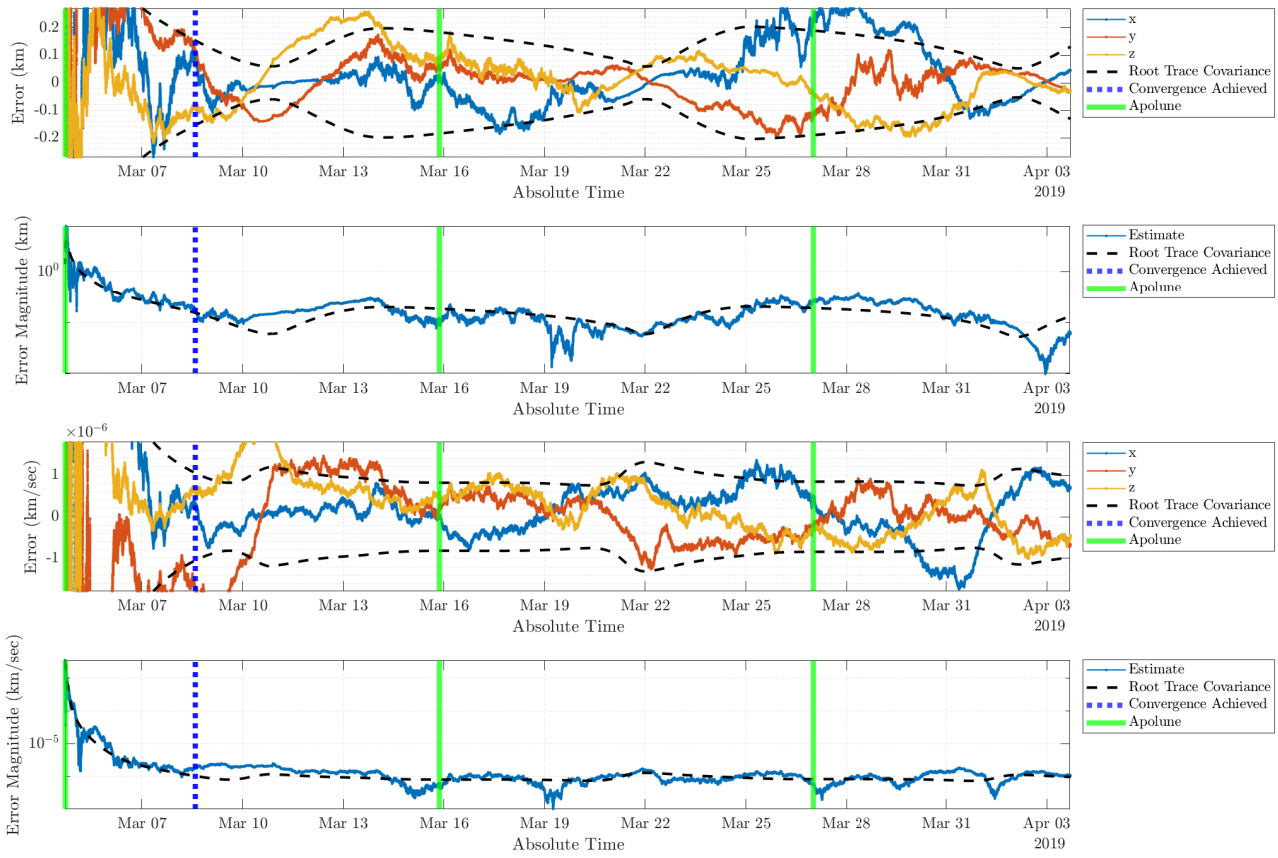

Figure A.15: Lunar Mirror Method Results for Case 3

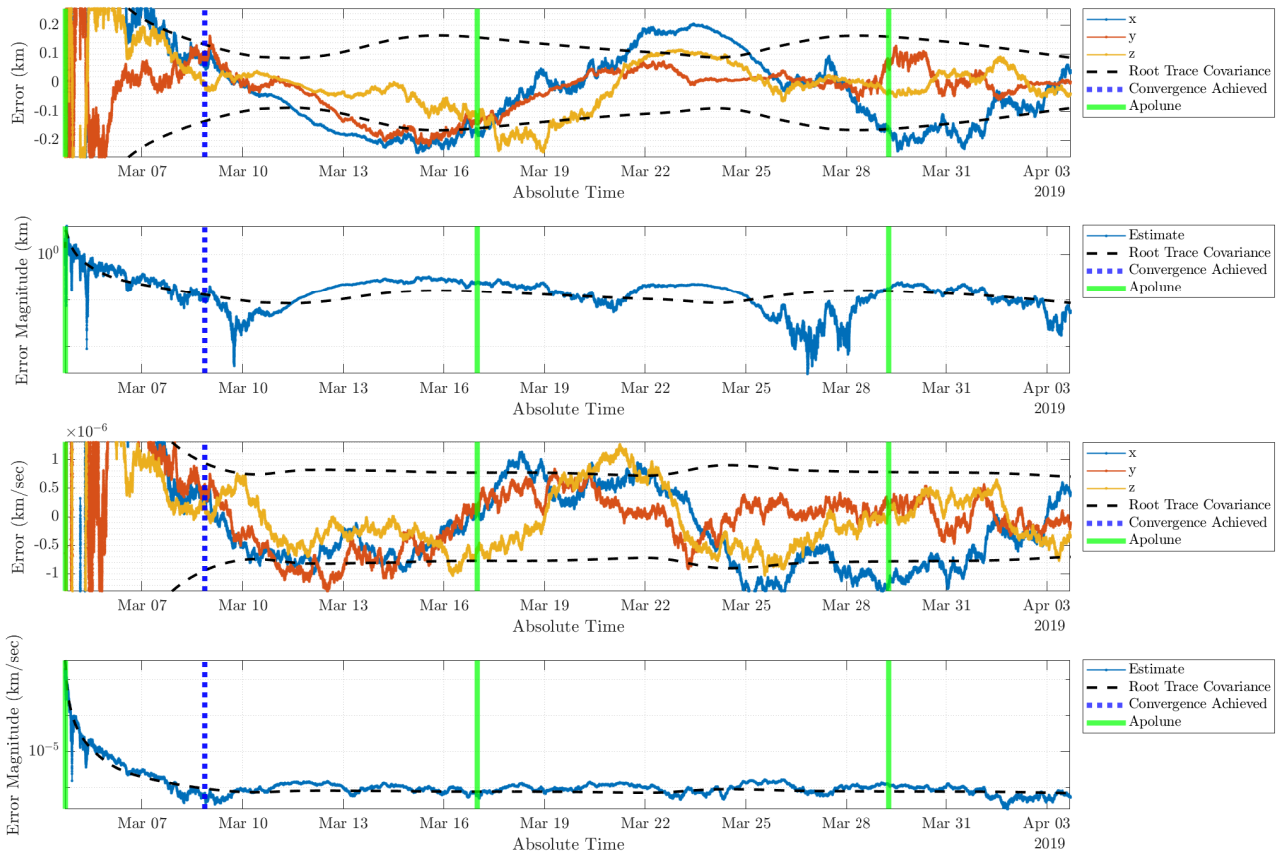

Figure A.16: Lunar Mirror Method Results for Case 4

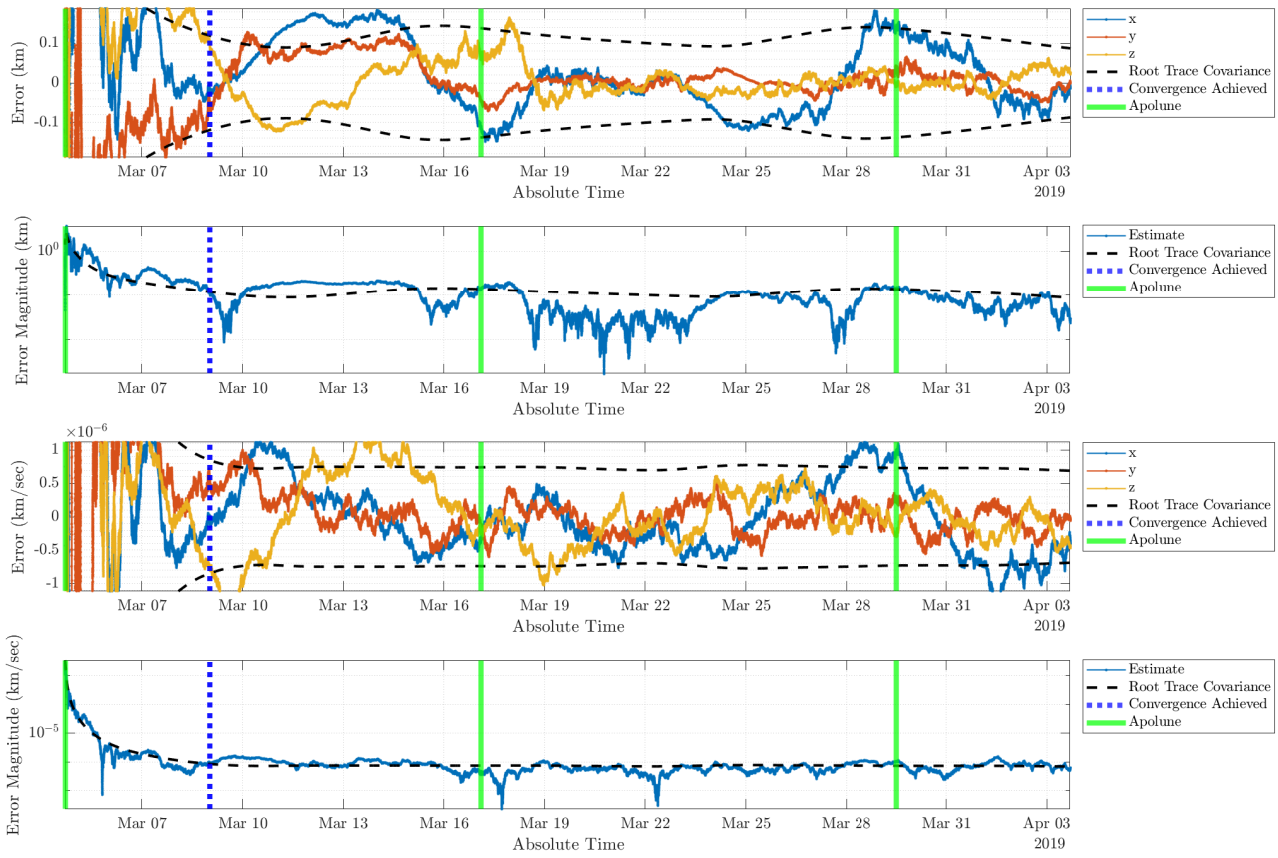

Figure A.17: Lunar Mirror Method Results for Case 5

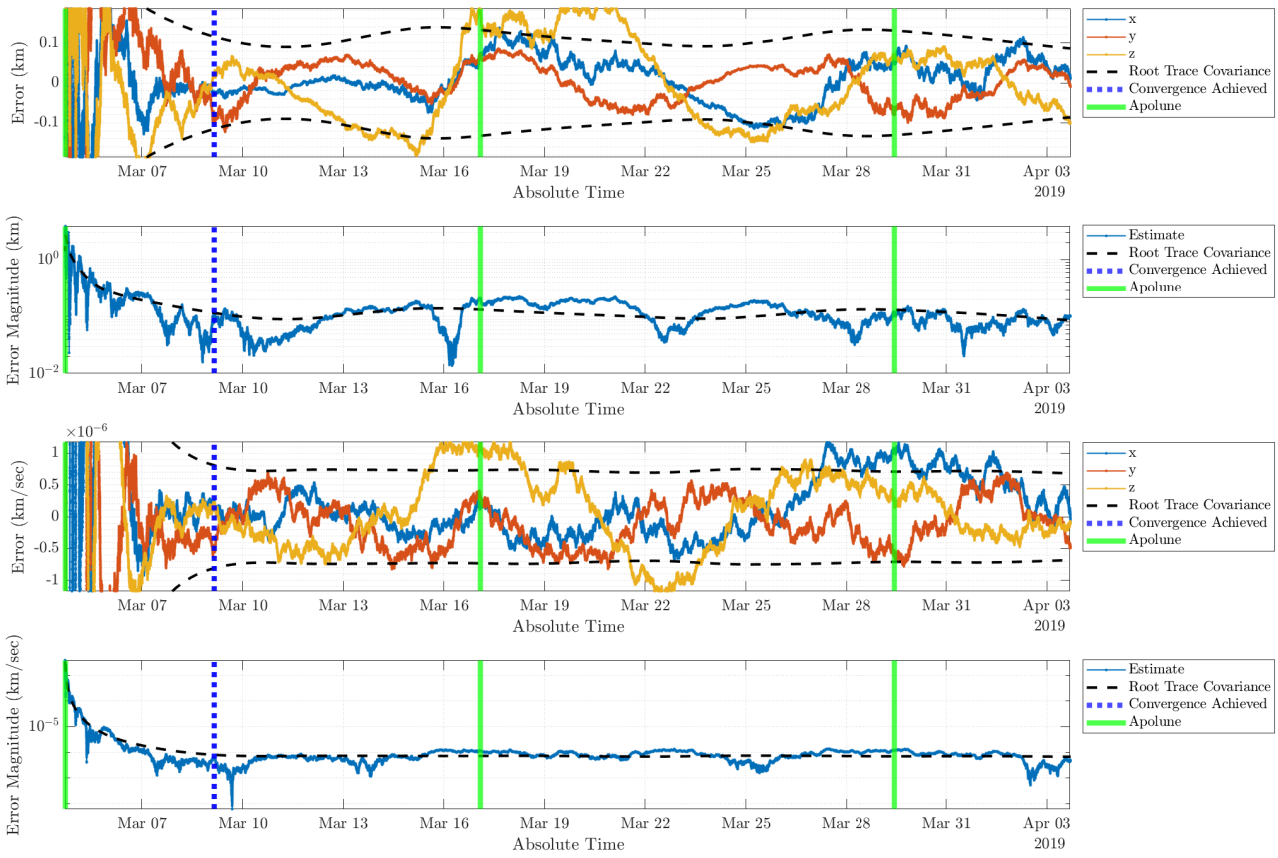

Figure A.18: Lunar Mirror Method Results for Case 6

Bibliography

[1] Blue ghost mission 1. URL https://fireflyspace.com/missions/blue-ghost-mission-1/. Online; accessed 30-April-2025.

[2] The circular restricted three–body problem. URL https://people.unipi.it/tommei/wp-content/uploads/sites/124/2021/08/3body.pdf. [Online; accessed 22-April-2025].

[3] About the deep space network. URL https://web.archive.org/web/20120603140725/http://deepspace.jpl.nasa.gov/dsn/about.html. [Online; accessed 30-April-2025].

[4] Gateway space station. URL https://www.nasa.gov/reference/gateway-about/. [Online; accessed 24-April-2025].

[5] After million-mile journey, james webb telescope reaches destination. URL https://www.nytimes.com/2022/01/24/science/james-webb-telescope-arrival.html. [Online; accessed 24-April-2025].

[6] Laser retroreflector: Diagram and photo. URL https://www.nist.gov/image/apollo15laserretroreflectorimageanddiagramjpg. Online; accessed 30-April-2025.

[7] Three-body periodic orbits. URL https://ssd.jpl.nasa.gov/tools/periodic_orbits.html. [Online; accessed 21-April-2025].

[8] fzero. URL https://www.mathworks.com/help/matlab/ref/fzero.html#btoc6lj-18.

[9] AGI. Construction of the stk star catalogs, . URL https://help.agi.com/stk/index.htm#stk/starConstruction.htm#BrightStar. [Online; accessed 21-April-2025].

[10] AGI. Basic constraints, . URL https://help.agi.com/stk/index.htm#stk/constraints-01.htm#los. [Online; accessed 21-April-2025].

[11] Danny Baird. Nasa explores upper limits of global navigation systems for artemis moon missions. January 2021. URL https://scitechdaily.com/nasa-explores-upper-limits-of-global-navigation-systems-for-artemis-moon-missions/. Source credits NASA for the graphic, but provides no further information.

[12] Divya Bhatia, Ulf Bestmann, and Peter Hecker. High accuracy attitude determination estimator system for irassi interferometer spacecraft. 02 2017.

[13] John Bowman and Mark Psiaki. Autonomous lunar orbit determination in support of a lunar positioning system. In *Proceedings of the 36th International Technical Meeting of the Satellite Division of The Institute of Navigation (ION GNSS+ 2023)*, pages 4016–4028, 10 2023. doi: 10.33012/2023.19427. URL https://doi.org/10.33012/2023.19427.

[14] Charlot, P., Jacobs, C. S., Gordon, D., Lambert, S., de Witt, A., Böhm, J., Fey, A. L., Heinkelmann, R., Skurikhina, E., Titov, O., Arias, E. F., Bolotin, S., Bourda, G., Ma, C., Malkin, Z., Nothnagel, A., Mayer, D., MacMillan, D. S., Nilsson, T., and Gaume, R. The third realization of the international celestial reference frame by very long baseline interferometry . *AA*, 644:A159, 2020. doi: 10.1051/0004-6361/202038368. URL https://doi.org/10.1051/0004-6361/202038368.

[15] John A. Christian. Optical navigation using planet's centroid and apparent diameter in image. *Journal of Guidance, Control, and Dynamics*, 38(2):192–204, 2015. doi: 10.2514/1.G000872. URL https://doi.org/10.2514/1.G000872.

[16] Daniel DeSlover. General lidar equation, 1996. URL https://lidar.ssec.wisc.edu/papers/dhd_thes/node10.htm. [Online; accessed 30-April-2025].

[17] Christopher D'Souza and Renato Zanetti. Navigation design and analysis for the orion earth-moon mission. Technical report, NASA, 2014. URL https://sites.utexas.edu/renato/files/2022/05/Navigation_Analysis_Cislunar_EM1_FINAL.pdf.

[18] Jeff Foust. Nasa deep space network reaches "critical point" as demand grows. URL https://spacenews.com/nasa-deep-space-network-reaches-critical-point-as-demand-grows/. [Online; accessed 23-April-2025].

[19] Marianne Guenot. There's no gps on the moon. nasa and esa have to fix that before humans return in 2 years. 2023. URL https://www.businessinsider.com/no-gps-on-moon-nasa-esa-artemis-plans-to-fix-2023-1. [Online; accessed 23-April-2025].

[20] Keric Hill and George H. Born. Autonomous interplanetary orbit determination using satellite-to-satellite tracking. *Journal of Guidance, Control, and Dynamics*, 30(3): 679–686, 2007. doi: 10.2514/1.24574. URL https://doi.org/10.2514/1.24574.

[21] Rebecca Inman, Greg Holt, John Christian, Kyle W. Smith, and Christopher D'Souza. *Artemis I Optical Navigation System Performance*. doi: 10.2514/6.2024-0514. URL https://arc.aiaa.org/doi/abs/10.2514/6.2024-0514.

[22] F. MARKLEY. *Autonomous navigation using landmark and intersatellite data*. doi: 10.2514/6.1984-1987. URL https://arc.aiaa.org/doi/abs/10.2514/6.1984-1987.

[23] Brooks McKinney. Navigating mars and beyond. URL https://www.

northropgrumman.com/space/navigating-mars-and-beyond-with-ln-200-inertial-measureme
[Online; accessed 23-April-2025].

[24] Jatan Mehta. Chandrayaan-3 makes historic touchdown on the moon. August 2023. URL https://www.scientificamerican.com/article/chandrayaan-3-makes-historic-touchdown-on-the-moon/. Online; accessed 30-April-2025.

[25] D. Michaels and J. Speed. Ball aerospace star tracker achieves high tracking accuracy for a moving star field. In *2005 IEEE Aerospace Conference*, pages 1–7, 2005. doi: 10.1109/AERO.2005.1559572.

[26] Heather Monaghan. What is the deep space network? 2020. URL https://www.nasa.gov/directorates/somd/space-communications-navigation-program/what-is-the-deep-space-network/.

[27] George Parks. Global positioning system (gps). URL https://slideplayer.com/slide/13752625/. Online, accessed 2025-05-01.

[28] Ryan Porzeinski. Feasibility of lunar laser ranging for autonomous cislunar spacecraft navigation. Master of Science in Aerospace Engineering Non-Thesis Final Project, 2024.

[29] Mark Psiaki. Aoe 5784 lecture 36. University Lecture, 2022.

[30] Mark Psiaki and Joanna Hinks. *Autonomous Lunar Orbit Determination Using Star Occultation Measurements*. 2007. doi: 10.2514/6.2007-6657. URL https://arc.aiaa.org/doi/abs/10.2514/6.2007-6657.

[31] Mark L. Psiaki. Autonomous orbit determination for two spacecraft from relative position measurements. *Journal of Guidance, Control, and Dynamics*, 22(2):305–312, 1999. doi: 10.2514/2.4379. URL https://doi.org/10.2514/2.4379.

[32] Arnold Reinhold. Apollo imu at draper hack the moon exhibit, September 2019. URL https://commons.wikimedia.org/w/index.php?curid=82248569. [Online; accessed 30-April-2025].

[33] Ronald W. Schafer. What is a savitzky-golay filter? [lecture notes]. *IEEE Signal Processing Magazine*, 28(4):111–117, 2011. doi: 10.1109/MSP.2011.941097.

[34] Emily Spreen, Kathleen Howell, and Diane Davis. Near rectilinear halo orbits and their application in cis-lunar space. 05 2017.

[35] R. V. Wagner, E. J. Speyerer, K. N. Burns, J. Danton, and M. S. Robinson. Revised coordinates for apollo hardware. *The International Archives of the Photogrammetry, Remote Sensing and Spatial Information Sciences*, XXXIX-B4: 517–521, 2012. doi: 10.5194/isprsarchives-XXXIX-B4-517-2012. URL https://isprs-archives.copernicus.org/articles/XXXIX-B4/517/2012/.

[36] Luke B. Winternitz, William A. Bamford, Samuel R. Price, J. Russell Carpenter, Anne C. Long, and Mitra Farahmand. Global positioning system navigation above 76,000 km for nasa's magnetospheric multiscale mission. *NAVIGATION*, 64(2):289–300, 2017. doi: https://doi.org/10.1002/navi.198. URL https://onlinelibrary.wiley.com/doi/abs/10.1002/navi.198.

[37] Luyuan Xu. How china's lunar relay satellite arrived in its final orbit, 06 2018. URL https://www.planetary.org/articles/20180615-queqiao-orbit-explainer. [Online; accessed 24-April-2025].

[38] Matthew P. Zaffram. Lunar laser ranging for autonomous cislunar spacecraft navigation. Master's thesis, Virginia Polytechnic Institute and State University, 2023.